Asian Power Electronics Journal

PERC, HK PolyU

First edition April 2021 Printed in Hong Kong by Reprographic Unit.
The Hong Kong Polytechnic University

Published by
Power Electronics Research Centre
The Hong Kong Polytechnic University
Hung Hom, Kowloon, Hong Kong

ISSN 1995-1051

Editorial board

Honorary Editor

Prof. Fred C. Lee, Electrical and Computer Engineer, Virginia Polytechnic Institute and State University

Editor

Victor Electronic Ltd.

Associate Editors and Advisors

Prof. Philip T. Krien
Department of Electrical and Computer Engineering, University of Illinois

Prof. Keyue Smedley
Department of Electrical and Computer Engineering, University of California

Prof. Muhammad H. Rashid
Department of Electrical and Computer Engineering, University of West Florida

Prof. Dehong Xu
College of Electrical Engineering, Zhejiang University

Prof. Hirofumi Akagi
Department of Electrical Engineering, Tokyo Institute of Technology

Prof. Xiao-zhong Liao
Department of Automatic Control, Beijing Institute of Technology

Prof. Hao Chen
Department of Automation, China University of Mining and Technology

Prof. Danny Sutanto
Integral Energy Power Quality and Reliability Centre, University of Wollongong

Prof. S.L. Ho
Department of Electrical Engineering, The Hong Kong Polytechnic University

Prof. Eric K.W. Cheng
Department of Electrical Engineering, The Hong Kong Polytechnic University

Dr. Norbert C. Cheung
Department of Electrical Engineering, The Hong Kong Polytechnic University

Dr. Edward W.C. Lo
Department of Electrical Engineering, The Hong Kong Polytechnic University

Dr. Martin H. L. Chow
Department of Electrical Engineering, The Hong Kong Polytechnic University

Dr. Chi Kwan Lee
Department of Electrical and Electronic Engineering, The University of Hong Kong

Table of Content

Four-wheel Anti-lock Braking System with Road Condition Detection Module

Jinhong Sun.[1] Ka Wai Eric Cheng.[2]
[1,2]Power Electronics Research Centre, The Hong Kong Polytechnic University, Hong Kong
E-mail: jinhong.sun@connect.polyu.hk[1] eric-cheng.cheng@polyu.edu.hk[2]

Abstract –The anti-lock braking system (ABS) designed based on the wheel slip control (WSC) method becomes more and more popular, especially after the in-wheel technology (IWT) is developed. With the help of IWT, a four-wheel braking control algorithm based on the robust fuzzy sliding mode WSC method is proposed. It mainly focuses on improving the robustness of the braking performance under complex road conditions, the steady-state achievement, and the reduction of the tracking error. The novelty is that the road condition detection module is added, which provides the road conditions to the ABS controller through acceleration training. This proposed four-wheel ABS is validated with enough robustness in dealing with complex road conditions through the simulation.

Keywords - anti-lock braking system, wheel slip control, in-wheel motor, road condition detection module

I. INTRODUCTION

Nowadays, many control strategies have been used to develop the anti-lock braking controller, which mainly including two types: the wheel acceleration-based control method and the wheel slip-based control method. The wheel acceleration-based one indirectly controls the wheel slip by controlling the wheel's deceleration or acceleration through brake pressure from a brake actuator. And the control algorithm with a logic threshold acceleration was developed and widely utilized in the ABS manufacturing industry [1]. However, this kind of ABS controller has some drawbacks on robust control as it largely depends on the experience of pre-setting the control thresholds [2]. Therefore, the wheel slip-based control method becomes more and more popular, especially with the development of IWT [3, 4]. Many control algorithms have been used to improve the control performance, such as the optimal wheel slip-based localization through the use of the proportional-integral-derivative (PID) method, the fuzzy method, and the neural network method [5].

Even though the hydraulic-based brake actuator is widely used in the automobile industry, the latest automotive electrification and automation trends still have some new challenges [6] with the optimization of WSC-based ABS. Despite the significant progress of ABS that has taken place over the last few years, with the current high demand in autonomous driving, smart control, and electric vehicle, new issues that constitute an open topic for research emerge. Among them, when braking on complex roads, the controller's robustness, steady-state performance and accuracy of tracking error need to be further studied, especially for designing a vehicle's four-wheel ABS. Different research activities are focused on the electro-hydraulic (EHB) brakes, and some research activities have been successfully implemented in the lab for a variety of EVs [2, 7].

Furthermore, another set-back is that modern and future generations of electric vehicles require the anti-lock braking controller to provide sufficient robustness for various road conditions. Recently, many control algorithms are used to build the required braking controller, such as the linear one: PID control [8], fuzzy logic control [9], and the nonlinear one: the sliding mode [10]. As the in-wheel motor is directly fixed inside the wheel, the proposed nonlinear anti-lock braking controller can adjust the braking force quickly to deal with the disturbances [11]. Generally, the significant difficulty involved in the design of the ABS is that the control performance depends strongly on the knowledge of the wheel and road characteristics, and the optimal wheel slip varies significantly with the road conditions. Besides, the real-time wheel slip depends on the wheel speed measured by the speed sensor, and vehicle velocity estimated by vehicle model; thus, the wheel slip is chosen as the direct control object of most anti-lock braking controllers [12]. The wheel speed is changed by adjusting the brake torque, thus, the real-time wheel slip is controlled within the expected range based on the road conditions [13].

II. ANALYSIS OF THE VEHICLE DYNAMICS

Table I shows the parameters of the established vehicle model, where, $(i = 1, 2, 3, 4)$ represent the left-front, right-front-right, left-rear, right-rear-right wheels, respectively. Other parameters are given in Table 1.

Table 1: Parameters of the ABS model

Sign	Description
μ_{r_i}	Rolling friction coefficient
$M(kg)$	Full mass of the vehicle
$R_w = 0.2768(m)$	Radius of the single wheel
$m_w = 12(kg)$	Single wheel weight
$J = 0.92(kg/m^2)$	Inertia of the single wheel
$\rho = 1.25(kg/m^3)$	Air density
$C_{air} = 0.23$	Air resistance coefficient
$A_{air} = 2.37(m^2)$	Air resistance area
$F_{b_r} = 11(kN)$	Rated braking force

A. Dynamical analyses of vehicle

The dynamic characteristics: the single wheel and the whole vehicle are formulated in (1), respectively. Actually, there have some forces that effect the control accuracy, such as the drag force from air F_{air} and the resistant force from the wheel rolling friction F_r. Therefore,

$$\begin{cases} \frac{d\omega_i}{dt} = \boldsymbol{A} = \frac{R_w}{J}\boldsymbol{F_f} - \frac{1}{J}\boldsymbol{T} \\ \frac{dv_{v_x}}{dt} = \dot{v}_{v_x} = -\frac{1}{M}\left[\boldsymbol{F_f}^T I + \boldsymbol{F_r}^T(\boldsymbol{I} - \boldsymbol{S_1}) + F_{air}\right] \end{cases} \tag{1}$$

Here, $\boldsymbol{A}$ is a matrix of $\dot{\omega}_i$, $\boldsymbol{S_1}$ and $\boldsymbol{T}$ are constructed by instant wheel data, describe λ_i and T_{b_i}, respectively.

$$\boldsymbol{A}=\begin{bmatrix}\dot{\omega}_1\\ \dot{\omega}_2\\ \dot{\omega}_3\\ \dot{\omega}_4\end{bmatrix},\qquad \boldsymbol{S_1}=\begin{bmatrix}\lambda_1\\ \lambda_2\\ \lambda_3\\ \lambda_4\end{bmatrix},\qquad \boldsymbol{T}=\begin{bmatrix}T_{b_1}\\ T_{b_2}\\ T_{b_3}\\ T_{b_4}\end{bmatrix} \tag{2}$$

Besides, $\boldsymbol{F_f}$ and $\boldsymbol{F_r}$ represent F_{f_i} and F_{r_i} , encompassing the real-time data at each sampling time for every single wheel (FL, FR, RL, and RR), respectively.

$$\boldsymbol{I}=\begin{bmatrix}1\\ 1\\ 1\\ 1\end{bmatrix},\qquad \boldsymbol{F_f}=\begin{bmatrix}F_{f_1}\\ F_{f_2}\\ F_{f_3}\\ F_{f_4}\end{bmatrix},\qquad \boldsymbol{F_r}=\begin{bmatrix}F_{r_1}\\ F_{r_2}\\ F_{r_3}\\ F_{r_4}\end{bmatrix} \tag{3}$$

Finally, the description of the forces mentioned above is summarized and shown in (4), where μ_i means the friction coefficient, and β_i stands for the force weight of each wheel.

$$\begin{cases} F_{f_i}=\frac{\mu_i\times M\times g}{\beta_i}\\ F_{r_i}=\frac{\mu_{r_i}\times M\times g}{\beta_i}\\ J=m_w\times R_w^2\\ F_{air}=0.5\times\rho\times C_{air}\times A_{air}\times v_{v_x}^2\end{cases} \tag{4}$$

B. Description of the wheel slip

According to the magic formula mentioned by Pacejka [13], which is used in MATLAB to simulate the braking operation and widely used in many literatures, four kinds of road conditions are demonstrated in Fig. 1. For the $\mu-\lambda$ friction curve shown in this figure, the dry, wet, snow, and icy roads can be divided based on the mathematical theory.

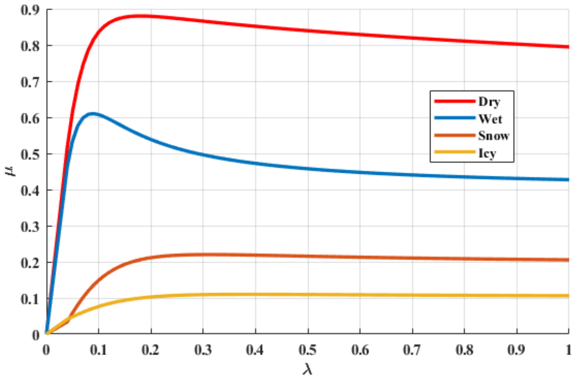

Fig.1 Four types of road conditions

For the wheel slip control method, the design target is the real-time wheel slip. Thus, the wheel slip dynamics can be obtained below,

$$\begin{cases} \lambda_i=\frac{v_{v_x}-\omega_i R_w}{v_{v_x}}\\ \frac{d\lambda_i}{dt}=\dot{\lambda}_i=-\frac{\dot{\omega}_i R_w-\dot{v}_{v_x}(1-\lambda_i)}{v_{v_x}}\end{cases} \tag{5}$$

Define $(\lambda_i,\dot{\lambda}_i)$ as the wheel slip characteristics, and S_2 to represent the $\dot{\lambda}_i$ characteristic. Therefore, (5) can be re-defined in (6).

$$\begin{cases} \boldsymbol{S_1}=\boldsymbol{I}-\frac{R_w}{v_{v_x}}\boldsymbol{W}\\ \boldsymbol{S_2}=-\frac{R_w}{v_{v_x}}\boldsymbol{A}+\frac{\dot{v}_{v_x}}{v_{v_x}}(\boldsymbol{I}-\boldsymbol{S_1})\end{cases} \tag{6}$$

Here, $\boldsymbol{W}$ stands for four wheels' ω_i at each sampling time, which can be measured through the wheel angular speed sensor.

$$\boldsymbol{W}=\begin{bmatrix}\omega_1\\ \omega_2\\ \omega_3\\ \omega_4\end{bmatrix},\qquad \boldsymbol{S_2}=\begin{bmatrix}\dot{\lambda}_1\\ \dot{\lambda}_2\\ \dot{\lambda}_3\\ \dot{\lambda}_4\end{bmatrix} \tag{7}$$

III. DESCRIPTION OF THE CONTROL METHOD

A. Road condition detection module

Fig. reveals the control detail of the proposed all-electric ABS. After a series of signal processing, the anti-lock braking controller's output signals and the associated braking torque requirement are transmitted back to the ECU and further transmitted by the ECU to the power controller to control the speed of the braking motor (also considered as the braking actuator).

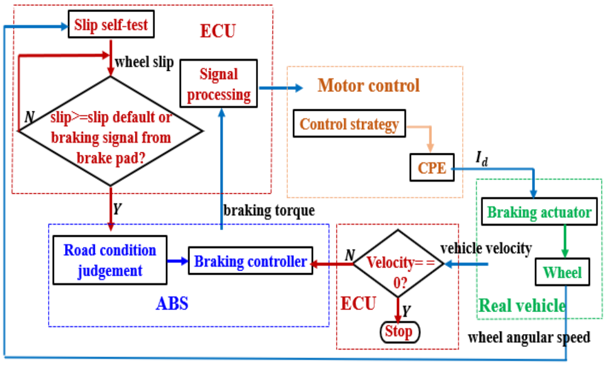

Fig.2 Control flow of the all-electric ABS

For the road condition detection module, the angular acceleration of every wheel is calculated at each sampling time under the initial braking force F_b during the calculation period Δt. Assume that, $F_b=0.4\times F_{b_r}$, and F_{b_r} is the rated braking force equals to $11kN$. F_b is applied at $t=0s$, and the angular wheel acceleration a_ω must be measured in the time window from t_1 to t_n with the specified sampling frequency $f=1kHz$. Define a_{ω_m} to represent the average of a_ω, thus,

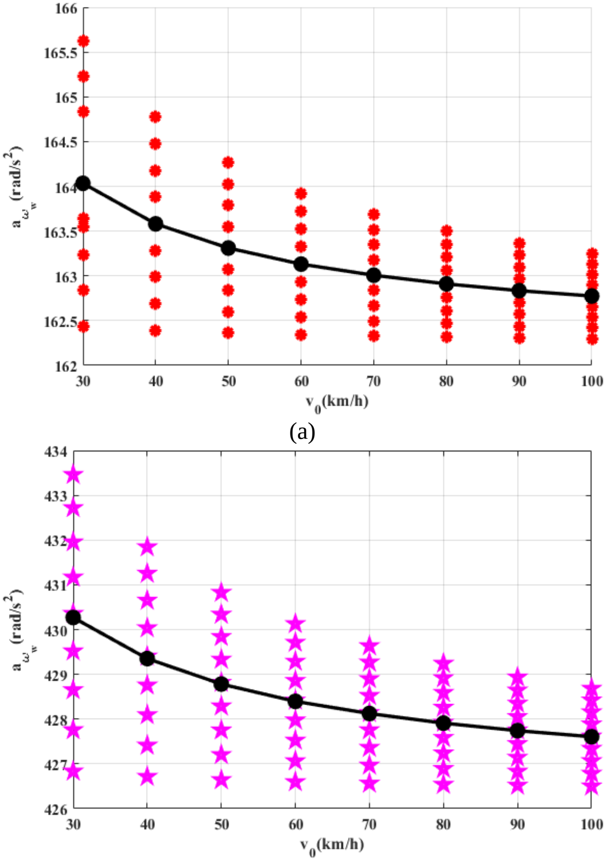

(a)

(b)

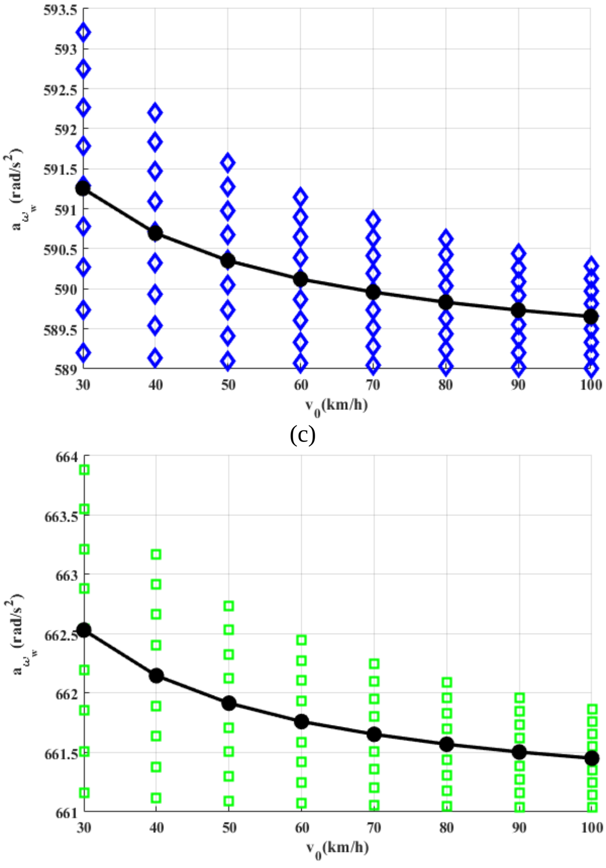

(c)

(d)

Fig.3 a_{ω_m} of the four types of road conditions (a) dry (b) wet (c) snow (d) icy

The acceleration indicators of the four typical roads are shown in Fig.3, and road condition judgement rules can be summarized below,

- If 164 $rad/s^2 \le a_\omega < 164\ rad/s^2$,
  the wheel is braking on the dry road, and the optimal wheel slip λ_o, the adhesion friction coefficient μ of the real road are in the dry condition curve shown in Fig.1.
- If 427 $rad/s^2 \le a_\omega < 430\ rad/s^2$,
  the wheel is braking on the wet road, and λ_o and μ are in wet condition curve shown in Fig.1.
- If 590 $rad/s^2 \le a_\omega < 591\ rad/s^2$,
  the wheel is braking on the snow road, and λ_o and μ are in snow condition curve shown in Fig.1.
- If 661 $rad/s^2 \le a_\omega < 663\ rad/s^2$,
  the wheel is braking on the icy road, and λ_o and μ are in icy condition curve shown in Fig.1.

The angular acceleration speed is considered as the preliminary basis for determining the road conditions. Next, λ_o and μ that generated by the above module are put into the braking controller.

B. Wheel slip

As well known, the operating principle can be concluded that through adjusting the braking torque to control the wheel speed, then affect the wheel slip. Based on (1), (4), and (5), the dynamic of wheel slip can be expressed in (8).

$$\dot{\lambda}_i = -\frac{1}{v_{v_x}}\{[\mu_i g + \mu_{r_i} g(1-\lambda_i)](1-\lambda_i)\} + \frac{T_{bw_i}}{v_{v_x} m_w R_w} \quad (8)$$

The control target of designed ABS can be obtained,

$$bT_{b_i} = \dot{\lambda}_i + \frac{1}{v_{v_x}}\left[\frac{F_{f_i}\beta_i(1-\lambda_i)}{M} + \frac{F_{r_i}(1-\lambda_i)}{m_w} + \frac{F_{air}(1-\lambda_i)}{M}\right] \quad (9)$$

C. Fuzzy sliding mode control

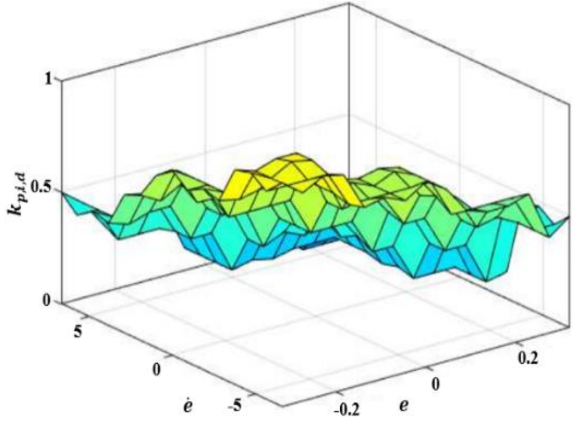

Fig.4 Fis of fuzzy controller's k_p, k_i and k_d

The algorithm of the anti-lock braking controller is built based on the fuzzy sliding mode WSC. The fuzzy function can easily incorporate the control experiences into the fuzzy controller through fuzzy rules, which reduces the difficulty of designing the controller. Define the error characteristic $e_i = \lambda_{o_i} - \lambda_i$, and its time derivative can be expressed as $\dot{e} = \frac{de_i}{dt} = \dot{\lambda}_{o_i} - \dot{\lambda}_i$. According to fuzzy rules of the fuzzy controller, PID variables can be yielded in Fig.4.

Then, variables of the fuzzy PID controller also considered as the input parameters of the fuzzy sliding mode controller can be obtained in (10). Where, k_{p,i,d_0} means the initial correction value of k_{p_0}, k_{i_0}, k_{d_0}.

$$K_{P,I,D_i} = k_{p,i,d}(e_i, \dot{e}_i) \times k_{p,i,d_0} \quad (10)$$

For the sliding mode controller, the sliding surface and its time derivates are set as,

$$\begin{cases} s = e + K_{P_i}\int e + K_{I_i}\iint e + K_{D_i}e \\ \dot{s} = \dot{e} + K_{P_i}e + K_{I_i}\int e + K_{D_i}\dot{e} \end{cases} \quad (11)$$

Based on the Lyapunov principle: $V = \frac{1}{2}s^2 \Longrightarrow \dot{V} = s\dot{s}$, FIS rules of this fuzzy sliding controller can be obtained and demonstrated in Fig.5.

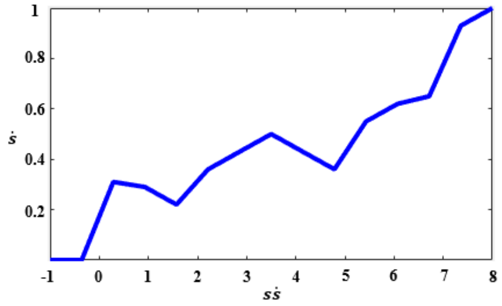

Fig.5 Fis of the sliding surface characteristic s and $\dot{s}$

IV. SIMULATION RESULTS

The vehicle model has been built based on the vehicle dynamics and the ABS control method, in which the straight-line case is chosen as the braking situation. Initial wheel slip λ_0 is set with a large value and are all done with the initial vehicle velocity $v_0 = 100km/h$.

Fig.6 shows the details of the vehicle braking on dry road conditions under the control of the four-wheel ABS controller. The whole adjustment of braking torque and velocities and the stop distance trend are given in Fig.6 (a). Parameters of the robust controller are shown in Fig.6 (b) and Fig.6 (c).

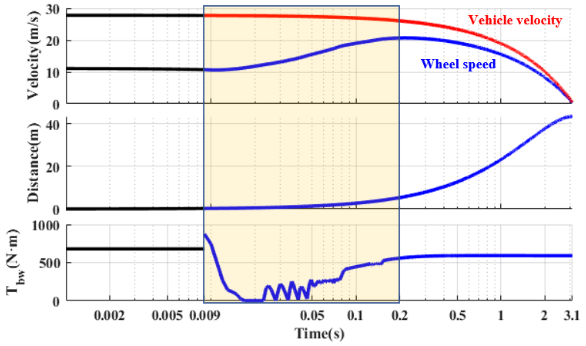

(a)

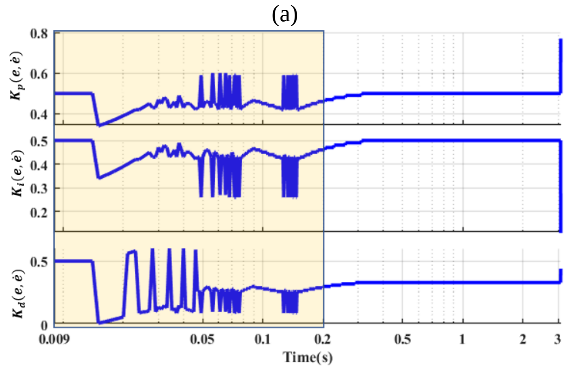

(b)

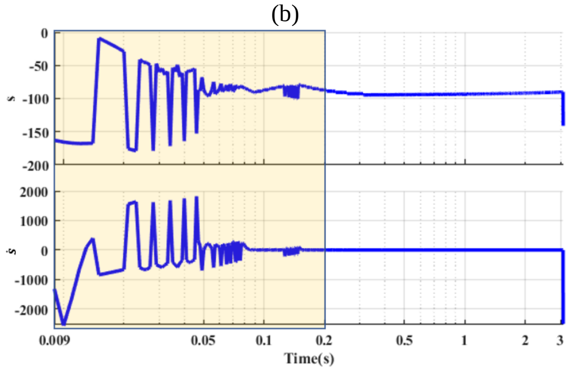

(c)

Fig.6 Control performance on dry road

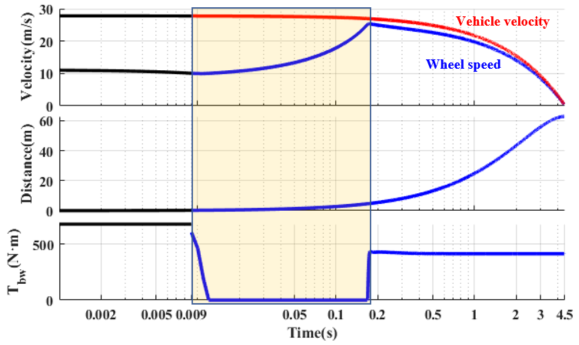

(a)

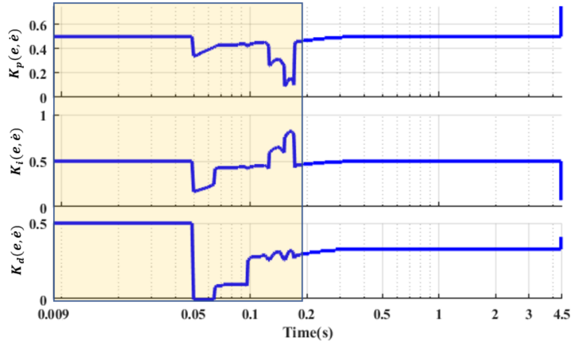

(b)

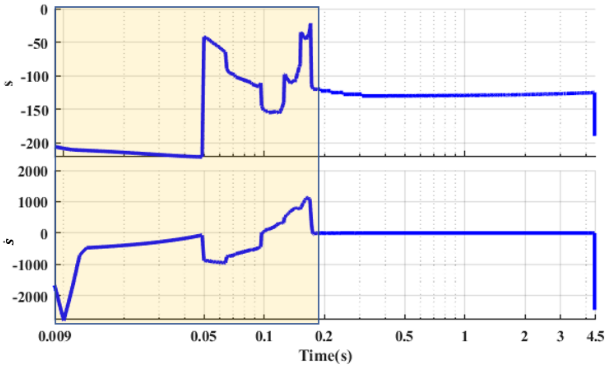

(c)

Fig.7 Control performance on wet road

During [0, 0.009]s, the vehicle is braking with the fixed braking force, and the road condition detection module operates to obtain the road information. Then these data can be transferred into the ABS controller, and ABS starts. The yellow shadow area represents the ABS control range with an obvious adjust function, and the smaller the range, the better the braking convergence. For dry roads, the braking stabilization time is controlled at about 0.2s.

Similarly, for the wet road condition, the vehicle still starts braking under the fixed braking force during 0.09s. After that, ABS operates to adjust the braking torque. Almost before 0.18s, the adjustment control reaches stable. Fig.8 and Fig.9 show the control performance details on snow and icy roads, respectively.

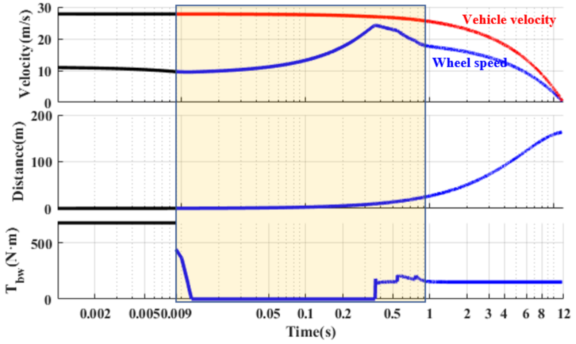

(a)

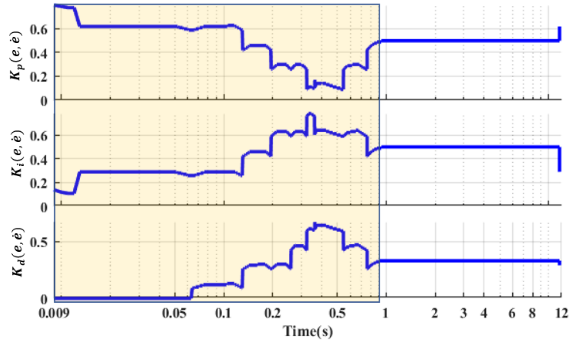

(b)

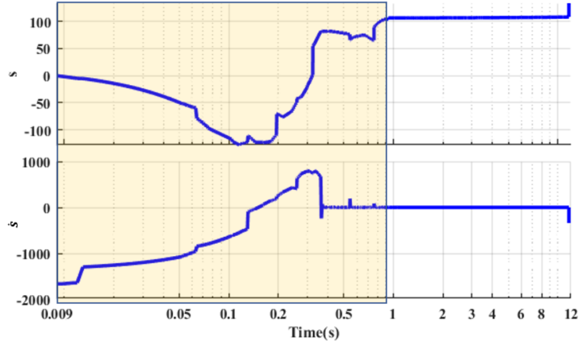

(c)

Fig.8 Control performance on snow road

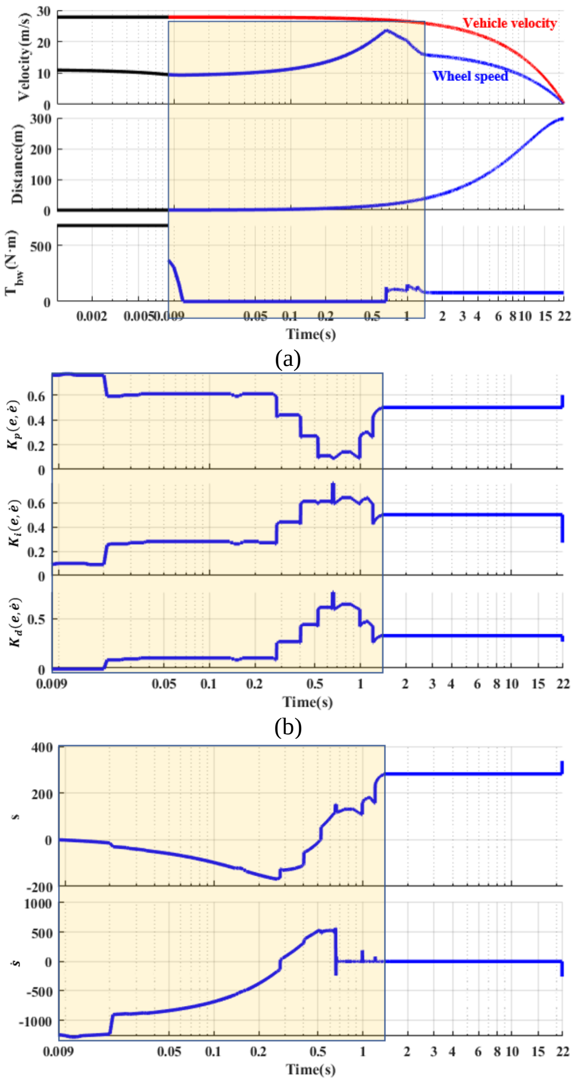

(a)

(b)

(c)

Fig.9 Control performance on icy road

For these two kinds of road conditions, the control performance is quite similar; however, the time to reach control stability has increased.

IV. Conclusion

In this paper, the anti-lock braking system with a road condition detection module for the four-wheel model is proposed, which is established based on the fuzzy sliding mode wheel slip control method. This proposed ABS controller is validated with enough robustness to deal with braking control on different road conditions through simulation. The road condition detection module works on providing road information to the ABS controller. This function improves the braking control accuracy and maintains the braking control achieving a stable state as soon as possible.

References

[1] X. D. Xue, K. W. E. Cheng, T. W. Ng and N. C. Cheung, "Multi-Objective Optimization Design of In-Wheel Switched Reluctance Motors in Electric Vehicles," IEEE Transactions on Industrial Electronics, vol. 57, no. 9, pp. 2980-2987, Sept. 2010.

[2] D. Savitski, D. Schleinin, V. Ivanov and K. Augsburg, "Robust Continuous Wheel Slip Control With Reference Adaptation: Application to the Brake System With Decoupled Architecture," IEEE Transactions on Industrial Informatics, vol. 14, no. 9, pp. 4212-4223, Sept. 2018.

[3] H. Jing, Z. Liu and H. Chen, "A Switched Control Strategy for Antilock Braking System With On/Off Valves," IEEE Transactions on Vehicular Technology, vol. 60, no. 4, pp. 1470-1484, May 2011.

[4] J. J. Castillo, J. A. Cabrera, A. J. Guerra and A. Simón, "A Novel Electrohydraulic Brake System With Tire–Road Friction Estimation and Continuous Brake Pressure Control," IEEE Transactions on Industrial Electronics, vol. 63, no. 3, pp. 1863-1875, March 2016

[5] Y. Chen, C. Tu and C. Lin, "Integrated electromagnetic braking/driving control of electric vehicles using fuzzy inference," IET Electric Power Applications, vol. 13, no. 7, pp. 1014-1021, July 2019.

[6] D. Tavernini *et al*., "An Explicit Nonlinear Model Predictive ABS Controller for Electro-Hydraulic Braking Systems," *IEEE Transactions on Industrial Electronics*, vol. 67, no. 5, pp. 3990-4001, May 2020

[7] A. Patil, D. Ginoya, P. D. Shendge and S. B. Phadke, "Uncertainty-Estimation-Based Approach to Antilock Braking Systems," IEEE Transactions on Vehicular Technology, vol. 65, no. 3, pp. 1171-1185, March 2016.

[8] H. Sun, J. Yan, Y. Qu and J. Ren, "Sensor fault-tolerant observer applied in UAV anti-skid braking control under control input constraint," Journal of Systems Engineering and Electronics, vol. 28, no. 1, pp. 126-136, Feb. 2017.

[9] W. Sun, J. Zhang and Z. Liu, "Two-Time-Scale Redesign for Antilock Braking Systems of Ground Vehicles," IEEE Transactions on Industrial Electronics, vol. 66, no. 6, pp. 4577-4586, June 2019.

[10] Y. Wang, H. Fujimoto and S. Hara, "Driving Force Distribution and Control for EV With Four In-Wheel Motors: A Case Study of Acceleration on Split-Friction Surfaces," IEEE Transactions on Industrial Electronics, vol. 64, no. 4, pp. 3380-3388, April 2017.

[11] X. Wu, M. Zhang and M. Xu, "Active Tracking Control for Steer-by-Wire System With Disturbance Observer," IEEE Transactions on Vehicular Technology, vol. 68, no. 6, pp. 5483-5493, June 2019.

[12] J. Ni, J. Hu and C. Xiang, "Envelope Control for Four-Wheel Independently Actuated Autonomous Ground Vehicle Through AFS/DYC Integrated Control," IEEE Transactions on Vehicular Technology, vol. 66, no. 11, pp. 9712-9726, Nov. 2017.

[13] J.H.Sun, X.D.Xue, K.W.E.Cheng, "Fuzzy Sliding Mode Wheel Slip Control for Smart Vehicle Anti-lock Braking System," Energies, vol. 12, no. 13, pp. 2501, 2019

Asian Power Electronics Journal, Vol. 15, No. 1, April 2021

An Investigation of Compensation Networks for Three-coil Wireless Power Transfer

WANG H.S.[1] CHENG K.W.E.[2] HU J.F.[3]

[1,2] Power Electronics Research Centre, Department of Electrical Engineering, The Hong Kong Polytechnic University, Hong Kong
[3] School of Engineering, Information Technology and Physical Sciences, Federation University, Australia
[1]E-mail: herschel.wang@connect.polyu.hk

Abstract –Wireless power transfer (WPT) can power loads over large air gaps with relatively high efficiency, offering an innovative and convenient charging way. Especially, three-coil WPT shows the superiority, namely, the extended transmission distance with high efficiency. However, compensation networks in three-coil WPT still necessitate investigation. In this paper, three compensation topologies including S-S-S, S-S-P and N-S-S are investigated. Some important characteristics including load-independent constant voltage (CV), load-independent constant current (CC) and zero voltage switching (ZVS) are concluded and compared among different topologies. Detailed design procedures of compensation networks based on three-coil couplers are demonstrated. The fundamental analysis, coil design, compensation topologies and experimental verification are all presented and discussed in this paper.

Keywords – Wireless power transfer, compensation topology, three-coil, constant output

I. INTRODUCTION

Wireless power transfer (WPT) is an outstanding technology that can transfer energy via time-varying magnetic fields [1]. Electrical apparatus equipped with WPT are able to beat conventionally contact-based methods because of no physical contact between from the source to the load. In other words, WPT can offer a versatile energization manner that gets rid of troubles from messy cables and the environmental constraint, which is gradually popular in electric vehicles [2, 3], heating systems [4, 5], light emitting diode (LED) driver [6, 7], consumer electronics [8] and mobile device [9, 10]. Considerable research efforts have been devoted to two-coil WPT due to its simplicity, which usually consists of one transmitter (Tx) and one receiver (Rx) [11-13]. In traditional two-coil WPT systems, there are basic four topologies, i.e., series–series (SS) [14], series–parallel (SP) [15], parallel–series (PS) [16], and parallel–parallel (PP) [17] as shown in Fig. 1.

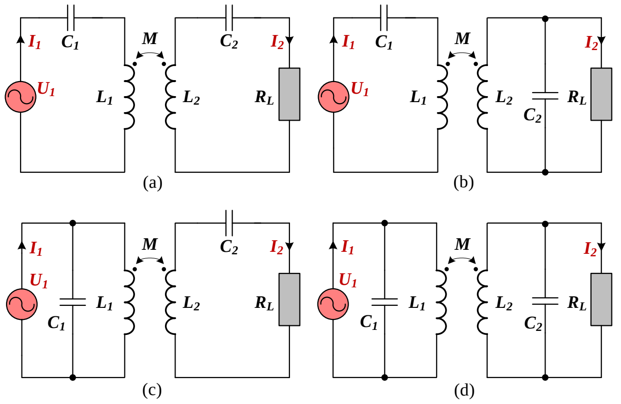

Fig. 1: Four basic compensation networks in two-coil WPT
(a) SS. (b) SP. (c) PS. (d) PP.

Recently, three-coil WPT is gaining increasing attention from researchers and engineers [18-21]. A typical three-coil WPT system consists of three coils, i.e., a transmitter (T_X), a relay coil and a receiver coil (R_X). In general, there are four typical types of three-coil WPT systems including type-A, B and C as shown in Fig. 2. The classification is according to the value of the mutual inductance between the Tx and the Rx, i.e., M_2 and the relevant positions of three coils. Detailed classification data is shown in Table. 1.

Table 1: One classification of three-coil WPT

Three-coil WPT with nonnegligible M_2	Three-coil WPT with negligible M_2		
TYPE-A	TYPE-B	TYPE-C	TYPE-D
[22, 23]	[24, 25]	[26, 27]	[7, 18, 19, 21, 28, 29]

Specifically, type A is the scenario with the nonnegligible M_2. By contrast, M_2 can be deliberately designed to be tiny enough to a negligible level from type B to D. Type B is the scenario where the relay coil is placed near the receiver. In type B, the load impedance is able to be reflected to obtain an optimal value, thereby realizing both arbitrary load impedance to the optimal value as well as high power delivery [24]. In terms of type C, the relay coil is placed to be equidistant between the transmitter and the receiver with the same distance to ensure expected mutual inductances [26] or the desired voltage gain [27].

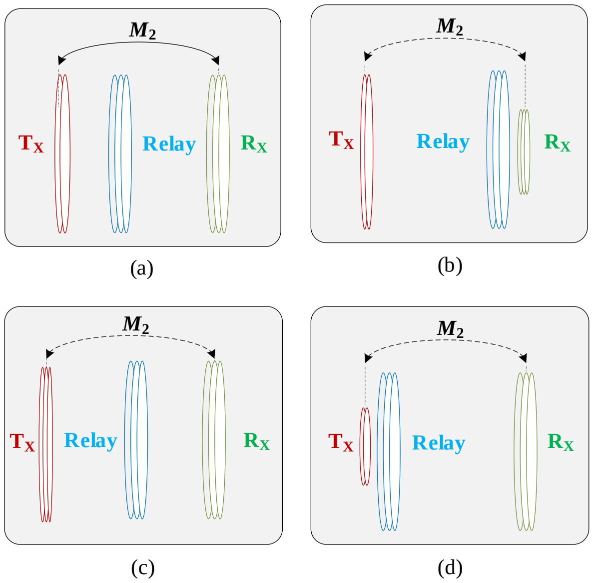

Fig. 2: Four typical types of three-coil WPT
(a) TYPE-A. (b) TYPE-B. (c) TYPE-C. (d) TYPE-D.

II. COUPLING STRUCTURE DESIGN

In this paper, only type D is considered and adopted owing to its intrinsic superiority, i.e., the extended transmission distance with high efficiency [13, 14]. One normal practice of type D is to shrink the size of transmitter coil with extended transmission distance to achieve an exceedingly small M_2. That means the influence from M_2 can be ignorable. Moreover, the relay coil from the type D saves room since it does not take up much space between the T_X and R_X compared to traditional two-coil structures [13]. Thus, the coupling structure in this paper consists of three coils in total, namely, transmitter, relay and receiver are demonstrated in Fig. 3. The airgap between T_X and relay is D_0 while the airgap between relay and R_X is D_1. Particularly, D represents the transmission distance from T_X to R_X, which is also the sum of D_0 and D_1.

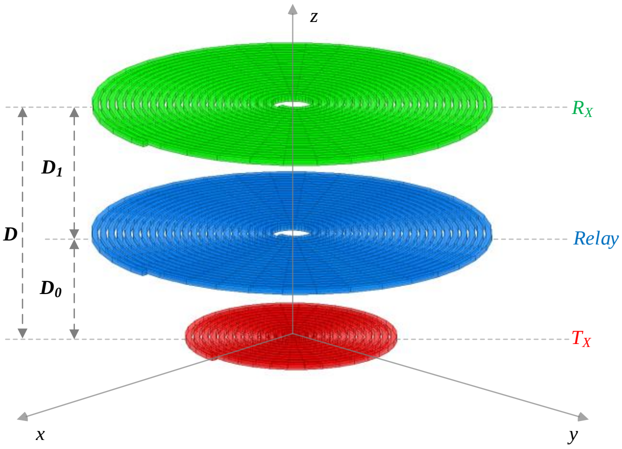

Fig. 3: The scheme of the coupling structure

As illustrated in Fig. 4, the parameters of these three coils are well designed by finite element analysis (FEA). Essential parameters are taken into consideration including inner diameter d_{in}, outer diameter d_{out}, wire diameter d_w, turn spacing S and turns N. Detailed parameter information from the magnetic coupling structure is able to be found in Table 2.

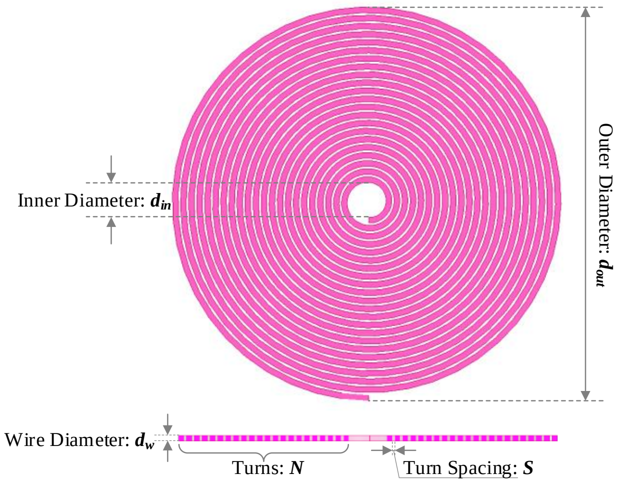

Fig. 4: The diagram of the coil design

Table 2: Detailed parameters of the coil design

Parameter Coil	d_{out} (mm)	d_{in} (mm)	d_w (mm)	S (mm)	N
T_X	75	10	2.1	0.663	12
Relay	20	20	2.1	0.895	22
R_X	150	150	2.1	0.895	22

III. CIRCUIT ANALYSIS

The circuit scheme of an entire three-coil WPT system is illustrated in Fig. 5. V_{dc} is the input dc voltage from regulated DC power supply. An inverter is adopted from the transmitter side to generate 200kHz AC power into the transmitter with an operating angular frequency ω. Specifically, L_1, L_r, and L_2 are the self-inductances of the T_X, the relay coil and the R_X with corresponding equivalent series resistances R_1, R_r and R_2 respectively [28]. The mutual inductance between the T_X and the relay coil is M_1 while the mutual inductance between the relay coil and the R_X is M_3. It is noteworthy that M_2, the mutual inductance between the T_X and the R_X, is delicately designed to be exceedingly small for simplifying analysis and reducing the cross-coupling effect. The fundamental component of the output voltage from the inverter can be expressed as [28]

$$u_1(t) = \frac{4V_{dc}}{\pi}\sin\omega t \tag{1}$$

The corresponding fundamental phasor can be given as

$$\dot{U}_1 = \frac{2\sqrt{2}}{\pi}V_{dc}\angle 0^\circ \tag{2}$$

A full-bridge rectifier is used after the receiver. R_{eq} denotes the equivalent load from the rectifier, which is gained as [28]

$$R_{eq} = \frac{8}{\pi^2}R_L \tag{3}$$

The output voltage on the load is represented by V_L. And U_O is the RMS value of the input voltage for the rectifier. The relationship between them can be expressed as

$$V_L = \frac{\pi U_O}{2\sqrt{2}} \tag{4}$$

Three compensation parts are also shown with related coils, which includes T_X compensation, relay compensation and R_X compensation. It is necessary to utilize compensation networks for minimizing VA rating and maximizing power transfer capability, achieving load-independent constant-voltage (CV) or current output (CC), improving efficiency and impeding bifurcation phenomenon [30]. Currently, the voltage-source inverter (VSI) is widely used for powering WPT systems, resulting in P compensation cannot be directly connected to the VSI [31]. Furthermore, relay coils tend to be simple and non-configurable, therefore, only S compensation can be connected with such a relay coil like [7], [28], [32]. Accordingly, three compensation types are concluded in Table.2, including S-S-S, S-S-P and N-S-S compensation networks.

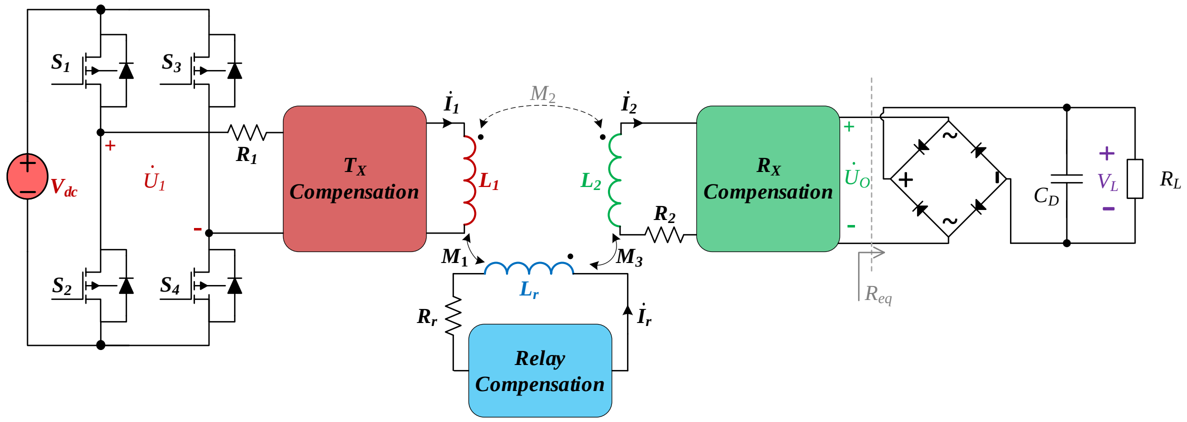

Fig. 5: The entire circuit scheme of the proposed three-coil WPT system

Table 2: Summary of compensation networks

Type	Equivalent Circuit Diagram
S-S-S	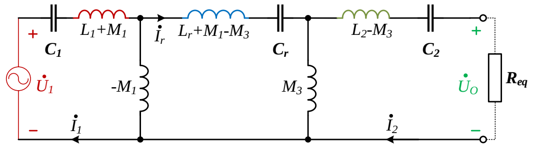
S-S-P	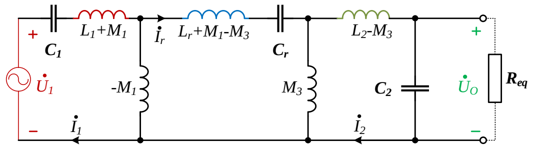
N-S-S	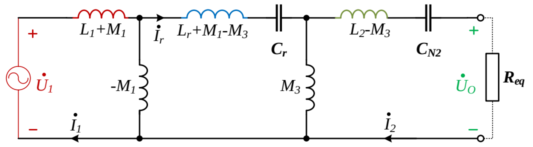

A. S-S-S Type

The S-S-S compensation topology is able to fulfill the load-independent output voltage [7, 28, 32]. For tuning the coils and achieving CV output, the operating angular frequency ω should meet the equation:

$$\omega = \sqrt{\frac{1}{L_1C_1}} = \sqrt{\frac{1}{L_rC_r}} = \sqrt{\frac{1}{L_2C_2}} \qquad (5)$$

According to [28], the voltage gain from the source to the equivalent load from S-S-S compensation topology can be written as

$$\frac{\dot{U}_1}{\dot{U}_O} = \frac{M_3}{M_1} \qquad (6)$$

By designing coupler deliberately, M_1 is equal to M_3 in this paper. Hence, the following relationship equations between the source part and the load side can be simplified and rewritten as

$$\dot{U}_O = \dot{U}_1 \qquad (7)$$

$$\dot{I}_O = \frac{\dot{U}_1}{R_{eq}} \qquad (8)$$

$$Z_{sss} = \dot{U}_1 / \dot{I}_1 = R_{eq} \qquad (9)$$

B. S-S-P Type

For tuning the coils and achieving CC output, the operating angular frequency ω should satisfy the equation (5) too. Then voltage relationship between the source part and the load side can be yielded:

$$\dot{U}_O = \frac{R_{eq}}{j\omega L_2}\dot{U}_1 \qquad (10)$$

The output current flowing through R_{eq} can be derived as

$$\dot{I}_O = \frac{\dot{U}_1}{j\omega L_2} \qquad (11)$$

The value of this output current is associated with the operating frequency ω, the self-inductance value of the R_X, and output voltage of the inverter. That means it is desirable to gain the objective output current by designing component parameters deliberately. And the input impedance of S-S-P is able to be gained as

$$Z_{ssp} = \dot{U}_1 / \dot{I}_1 = \frac{\omega^2 {L_2}^2 R_{eq}}{{R_{eq}}^2 + \omega^2 {L_2}^2} + j\frac{\omega^3 {L_2}^3}{{R_{eq}}^2 + \omega^2 {L_2}^2} \qquad (12)$$

It is noted that there is an imaginary component in Z_{ssp}, thereby making the whole system inductive and improving the VA rating.

C. N-S-S Type

The N from N-S-S represents there is no compensation network from the transmitter part in this topology. Then, the compensation network from the receiver part should take the responsibility for tuning the transmitter part [33]. Therefore, the capacitor in the receiver side C_{N2} can be expressed as

$$C_{N2} = \frac{1}{\omega^2 (L_1 + L_2)} \qquad (13)$$

Similarly, the load-independent output voltage can be gained as

$$\dot{U}_O = \dot{U}_1 \qquad (14)$$

This voltage is only related to the output voltage from the inverter. Then, the current flowing through R_{eq} can be derived as

$$\dot{I}_O = \frac{1}{R_{eq}}\dot{U}_1 \tag{15}$$

Therefore, the input impedance of N-S-S network can be expressed as

$$Z_{nss} = \dot{U}_1 / \dot{I}_1 = R_{eq} \tag{16}$$

IV. EXPERIMENTAL VALIDATION

An experimental platform has been built up to validate the availability of the theoretical analysis as illustrated in Fig.6. All the coils are made of 250-strand LITZ wire to form inductors, which dramatically reduces the skin effect. The operating frequency from the inverter is set to be 200kHz. One switch and two resistive loads are used to verify transient response when the load change happens. Experimental waveforms are directly gained and analyzed from oscilloscope Tektronix MDO3024. The two output channels from power supply EZ Digital GP-1305DU are connected in series to constantly provide 50V as the DC input voltage to feed the inverter. And the measured parameters of the entire prototype are shown in Table. 3.

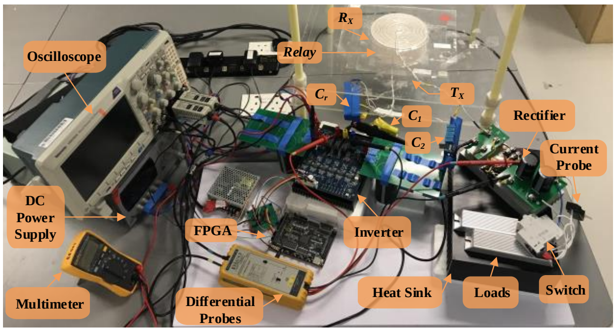

Fig. 6: Experimental Prototype

Table 3: Measured parameters

L_1	L_r	L_2	M_1	M_3
4.63μH	32.62μH	29.51μH	4.65μH	4.65μH
C_1	C_r	C_2	C_{N2}	f
137.05nF	19.32nF	21.10nF	18.47nF	200kHz
R_1	R_r	R_2	D_0	D_1
0.04Ω	0.20Ω	0.17Ω	0.5cm	6.5cm

A. S-S-S Experimental Results

Fig. 7 depicts the essential waveforms from the inverter and the output voltage on the load part. It is noteworthy that the current slightly lags corresponding voltage, which indicates ZVS can be achieved in this topology.

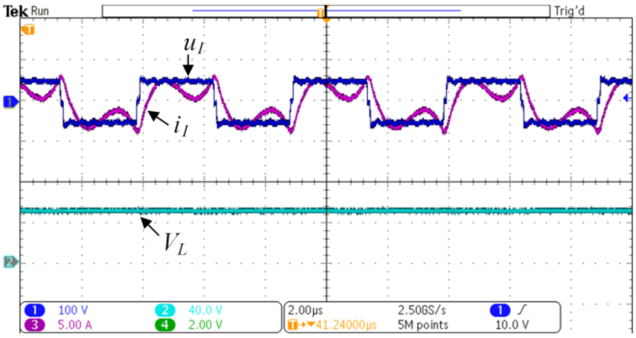

Fig. 7: Essential waveforms from the inverter and the output voltage on the load in S-S-S type

Fig. 8 demonstrates the transient response of S-S-S topology. Even though the output current from the load experiences a sharp rise and down, the output voltage keeps stable around 50V. Indicated by the oscilloscope, the change of voltage is 2.4V. In other words, the voltage fluctuation is 4.8% from 50.4 V to 48V while the load drops by 50%.

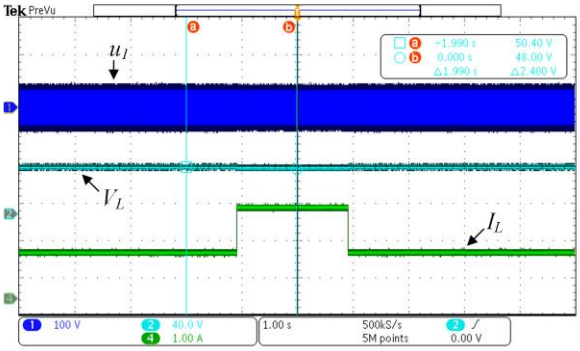

Fig. 8: Transient response when the load is changed from 40Ω to 20Ω and back to 40Ω in S-S-S type

B. S-S-P Experimental Results

Fig. 9 illustrates the essential waveforms from the inverter at the T_X side and the output voltage on the load. Nevertheless, the equivalent impedance is inductive so that i_1 lags u_1 around 90 degrees. Therefore, the reactive power cannot be ignored in this topology.

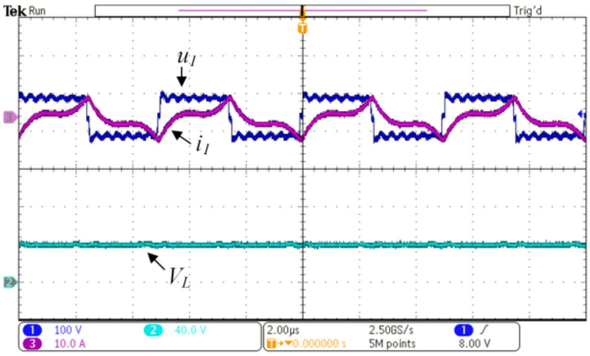

Fig. 9: Essential waveforms from the inverter and the output voltage on the load in S-S-P type

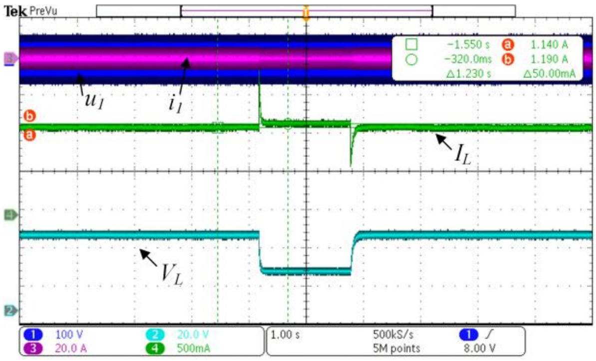

Fig. 10: Transient response when the load changes from 40Ω to 20Ω and back to 40Ω in S-S-P type

Fig. 10 manifests the measured waveforms of u_1, i_1, V_L and I_L when the load is between 40Ω and 20Ω, respectively. The current is changed from 1.19A to 1.14A with overshoots.

The oscillation of the current is 50mA. The output current declines by 4.2% and the load falls by 50%.

C. N-S-S Experimental Results

The steady-mode waveforms of u_1, i_1, V_L and I_L are shown in Fig. 11 at R_L=40Ω, which illustrates that the current i_1 slightly lags u_1. This manifests ZVS can also be achieved in this topology.

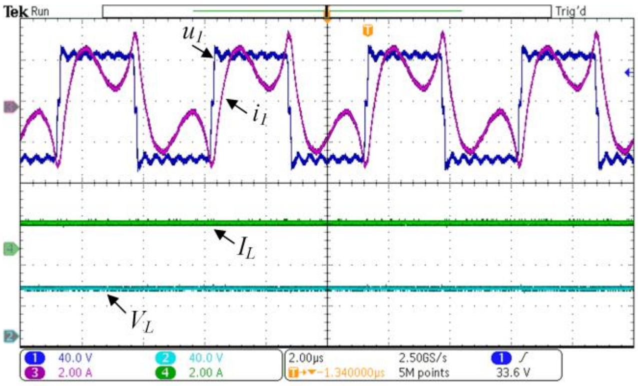

Fig. 11: Essential waveforms from the inverter and the output voltage on the load in N-S-S type

Fig.12 depicts the transient response of N-S-S topology. When the load is 40 Ω, the output voltage is 45.6V. Then the load is reduced to 20Ω, and the output voltage becomes 44.8V. The voltage change is only 0.8V, which can be directly detected from the oscilloscope. The output voltage declines by 1.8% and the load falls by 50%.

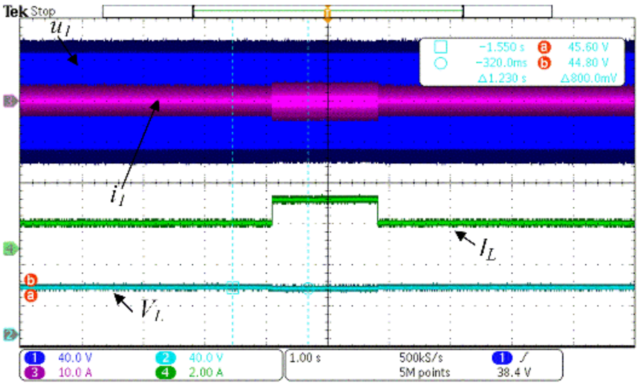

Fig. 12: Transient response when the load changes from 40Ω to 20Ω and back to 40Ω in N-S-S type

V. CONCLUSION

In this paper, three compensation networks, namely, S-S-S, S-S-P and N-S-S are studied for three-coil WPT systems. Coupling structure design, circuit analysis and experimental verification are all conducted to investigate key characteristics such as load-independent CC or CV outputs and ZVS. All coils are designed by the finite element analysis software carefully. A summary of the compensation network is also demonstrated with equivalent T-model circuits. Key waveforms with related description have been shown and discussed. An experimental prototype is managed to be built up and corresponding experimental results successfully show the agreement with the theoretical analysis. In the future, WPT systems equipped with these compensation networks could be scaled down or up for wirelessly charging consumer electronics or EVs.

REFERENCES

[1] Y. Li, J. Hu, K. W. Chan, K. W. E. Cheng, and M. Liu, "A Flexible Load-Independent Multi-Output Wireless Power Transfer System Based on Double-T Resonant Circuit Technique," in *2018 IEEE Energy Conversion Congress and Exposition (ECCE)*, 23-27 Sept. 2018 2018, pp. 3593-3596.

[2] K. W. K. Chen and K. W. E. Cheng, "Review of magnetic resonance technology, recent research trends and issues in EV wireless charging," in *The 11th IET International Conference on Advances in Power System Control, Operation and Management (APSCOM 2018)*, 11-15 Nov. 2018 2018, pp. 1-7.

[3] Y. C. Fong and K. W. E. Cheng, "A switched-capacitor step-up inverter for bidirectional wireless charging applications in electric microcar," in *2017 7th International Conference on Power Electronics Systems and Applications - Smart Mobility, Power Transfer & Security (PESA)*, 12-14 Dec. 2017 2017, pp. 1-6.

[4] L. Meng and K. W. E. Cheng, "Wireless power transfer technology for electric iron based on multi-coils induction heating design," *IET Power Electronics,* vol. 12, no. 10, pp. 2566-2577, 2019, doi: 10.1049/iet-pel.2018.6305.

[5] L. C. Meng, K. W. E. Cheng, and W. M. Wang, "Thermal Impacts of Electromagnetic Proximity Effects in Induction Cooking System With Distributed Planar Multicoils," *IEEE Transactions on Magnetics,* vol. 47, no. 10, pp. 3212-3215, 2011.

[6] Y. Li *et al.*, "Analysis, Design, and Experimental Verification of a Mixed High-Order Compensations-Based WPT System with Constant Current Outputs for Driving Multistring LEDs," *IEEE Transactions on Industrial Electronics,* vol. 67, no. 1, pp. 203-213, 2020.

[7] Y. Li, J. Hu, X. Li, H. Wang, and K. W. E. Cheng, "Cost-Effective and Compact Multistring LED Driver Based on a Three-Coil Wireless Power Transfer System," *IEEE Transactions on Power Electronics,* vol. 34, no. 8, pp. 7156-7160, 2019.

[8] X. Li, J. Hu, Y. Li, H. Wang, M. Liu, and P. Deng, "A Decoupled Power and Data-Parallel Transmission Method With Four-Quadrant Misalignment Tolerance for Wireless Power Transfer Systems," *IEEE Transactions on Power Electronics,* vol. 34, no. 12, pp. 11531-11535, 2019.

[9] X. Li, J. Hu, H. Wang, X. Dai, and Y. Sun, "A New Coupling Structure and Position Detection Method for Segmented Control Dynamic Wireless Power Transfer Systems," *IEEE Transactions on Power Electronics,* vol. 35, no. 7, pp. 6741-6745, 2020.

[10] Y. Li *et al.*, "A New Coil Structure and Its Optimization Design With Constant Output Voltage and Constant Output Current for Electric Vehicle Dynamic Wireless Charging," *IEEE Transactions on Industrial Informatics,* vol. 15, no. 9, pp. 5244-5256, 2019.

[11] X. Li, C. Tang, X. Dai, P. Deng, and Y. Su, "An Inductive and Capacitive Combined Parallel Transmission of Power and Data for Wireless Power Transfer Systems," *IEEE Transactions on Power Electronics,* vol. 33, no. 6, pp. 4980-4991, 2018.

[12] X. Dai, X. Li, Y. Li, and A. P. Hu, "Maximum Efficiency Tracking for Wireless Power Transfer Systems With Dynamic Coupling Coefficient Estimation," *IEEE Transactions on Power Electronics,* vol. 33, no. 6, pp. 5005-5015, 2018.

[13] D. Patil, M. K. McDonough, J. M. Miller, B. Fahimi, and P. T. Balsara, "Wireless Power Transfer for Vehicular Applications: Overview and Challenges," *IEEE Transactions on Transportation Electrification,* vol. 4, no. 1, pp. 3-37, 2018.

[14] Z. Zhang, H. Pang, A. Georgiadis, and C. Cecati, "Wireless Power Transfer—An Overview," *IEEE Transactions on Industrial Electronics,* vol. 66, no. 2, pp. 1044-1058, 2019.

[15] B. J. Varghese, A. Kamineni, and R. A. Zane, "Empirical Closed-Form Analysis for Inductance and Coupling Coefficient Calculation for Ferrite-Based Matched Inductive Charging Systems," in *2019 IEEE Energy Conversion Congress and Exposition (ECCE)*, 29 Sept.-3 Oct. 2019 2019, pp. 1210-1214.

[16] J. Haruna, U. D. Kavimandan, O. Onar, V. P. Galigekere, and J. Pries, "Sensitivity Analysis of Compensation Topologies for Dynamic WPT System," in *2020 IEEE Transportation Electrification Conference & Expo (ITEC)*, 23-26 June 2020 2020, pp. 284-289.

[17] A. Rakhymbay, M. Bagheri, and M. Lu, "A simulation study on four different compensation topologies in EV wireless charging," in *2017 International Conference on Sustainable Energy Engineering and Application (ICSEEA)*, 23-24 Oct. 2017 2017, pp. 66-73.

[18] J. Zhang, X. Yuan, C. Wang, and Y. He, "Comparative Analysis of Two-Coil and Three-Coil Structures for Wireless Power Transfer," *IEEE Transactions on Power Electronics,* vol. 32, no. 1, pp. 341-352, 2017.

[19] W. X. Zhong, C. Zhang, X. Liu, and S. Y. R. Hui, "A Methodology for Making a Three-Coil Wireless Power Transfer System More Energy Efficient Than a Two-Coil Counterpart for Extended Transfer Distance," *IEEE Transactions on Power Electronics,* vol. 30, no. 2, pp. 933-942, 2015.

[20] Q. Wang and Y. Wang, "Power efficiency optimisation of a three-coil wireless power transfer using compensatory reactance," *IET Power Electronics,* vol. 11, no. 13, pp. 2102-2108, 2018.

[21] Z. Jian, Y. Xinmei, and W. Chuang, "A study of three-coil magnetically coupled resonators for wireless power transfer," in *2015 IEEE International Wireless Symposium (IWS 2015)*, 30 March-1 April 2015 2015, pp. 1-4.

[22] L. Yang, X. Li, S. Liu, Z. Xu, C. Cai, and P. Guo, "Analysis and Design of Three-Coil Structure WPT System With Constant Output Current and Voltage for Battery Charging Applications," *IEEE Access,* vol. 7, pp. 87334-87344, 2019.

[23] G. Zhu and D. Gao, "Effects of intermediate coil on power transfer capability and efficiency in three-coil wireless power transfer system," in *2017 IEEE Transportation Electrification Conference and Expo, Asia-Pacific (ITEC Asia-Pacific)*, 7-10 Aug. 2017 2017, pp. 1-6.

[24] M. Kiani, U. Jow, and M. Ghovanloo, "Design and Optimization of a 3-Coil Inductive Link for Efficient Wireless Power Transmission," *IEEE Transactions on Biomedical Circuits and Systems,* vol. 5, no. 6, pp. 579-591, 2011.

[25] Y. Ota, T. Takura, F. Sato, and H. Matsuki, "Wireless power transfer by low coupling electromagnetic induction — LC booster," in *2012 IEEE MTT-S International Microwave Workshop Series on Innovative Wireless Power Transmission: Technologies, Systems, and Applications*, 10-11 May 2012 2012, pp. 175-178.

[26] Q. Vo, Q. Duong, and M. Okada, "Cooperative Transmission in Three-Coil Inductive Power Transfer System with Load-Independent Output Voltages," in *2019 International Workshop on Antenna Technology (iWAT)*, 3-6 March 2019 2019, pp. 225-227.

[27] K. B. S. Kiran, M. Kumari, R. K. Behera, O. Ojo, and A. Iqbal, "Analysis and experimental verification of three-coil inductive resonant coupled wireless power transfer system," in *2017 National Power Electronics Conference (NPEC)*, 18-20 Dec. 2017 2017, pp. 84-89.

[28] Y. Li, Q. Xu, T. Lin, J. Hu, Z. He, and R. Mai, "Analysis and Design of Load-Independent Output Current or Output Voltage of a Three-Coil Wireless Power Transfer System," *IEEE Transactions on Transportation Electrification,* vol. 4, no. 2, pp. 364-375, 2018.

[29] Y. Zhang, T. Lu, and Z. Zhao, "Reducing the impact of source internal resistance by source coil in resonant wireless power transfer," in *2014 IEEE Energy Conversion Congress and Exposition (ECCE)*, 14-18 Sept. 2014 2014, pp. 845-850.

[30] W. Zhang and C. C. Mi, "Compensation Topologies of High-Power Wireless Power Transfer Systems," *IEEE Transactions on Vehicular Technology,* vol. 65, no. 6, pp. 4768-4778, 2016.

[31] Y. Zhang, Z. Yan, Z. Liang, S. Li, and C. C. Mi, "A High-Power Wireless Charging System Using LCL-N Topology to Achieve a Compact and Low-Cost Receiver," *IEEE Transactions on Power Electronics,* vol. 35, no. 1, pp. 131-137, 2020.

[32] P. Darvish, S. Mekhilef, and H. A. Illias, "A Novel S-S-LCLCC Compensation for Three-Coil WPT to Improve Misalignment and Energy Efficiency Stiffness of Wireless Charging System," *IEEE Transactions on Power Electronics,* pp. 1-1, 2020.

[33] Y. Liu, R. Mai, D. Liu, Y. Li, and Z. He, "Efficiency Optimization for Wireless Dynamic Charging System With Overlapped DD Coil Arrays," *IEEE Transactions on Power Electronics,* vol. 33, no. 4, pp. 2832-2846, 2018.

Asian Power Electronics Journal, Vol. 15, No. 1, April 2021

A Compact Design for a Switchable Wireless Charger

WANG H.S.[1] CHENG K.W.E.[2] HU J.F.[3]

[1,2] Power Electronics Research Centre, Department of Electrical Engineering, The Hong Kong Polytechnic University, Hong Kong
[3] School of Engineering, Information Technology and Physical Sciences, Federation University, Australia
[1]E-mail: herschel.wang@connect.polyu.hk

Abstract –With the continuous miniaturization of electronic products, the compact structure of wireless power transfer (WPT) is extraordinarily necessary for consumer electronics. In addition, to meet the need in charging, load independent output current (CC) and constant output voltage (CV) are supposed to be taken into consideration since it is regarded as one of the most popular methods for charging batteries. This paper studies a switchable and compact design for a wireless charger. The compensation network can be changed between double LCL topology and LCL-S topology. Configurable CC and CV outputs can be achieved by adopting two switches without utilizing sophisticated control loops or any communication between the transmitter and the receiver. Compared with LCC compensation networks, the proposed special structure can save components under both double LCL and LCL-S conditions. The ferrite cores naturally take the responsibility as magnetic shielding for unwanted couplings in a such compact structure. This special design not only greatly alleviates the cross-coupling phenomenon but surely makes the compensation networks design straightforward as well. Ultimately, the fundamental analysis, the related mathematical derivation, detailed circuit topologies, switchable compensation designs and the experimental platform are all discussed and investigated. The proposed design is also analyzed and validated by experimental tests under different charging conditions.

Keywords – Wireless charging, inductive power transfer, compensation topology, switchable network, constant output

I. INTRODUCTION

Wireless power transfer (WPT) becomes increasingly attractive from researchers and engineers owing to its impressive benefits. For example, energy can be transferred without any mechanical contact over a relatively large gap. In other words, WPT can help electrical appliances gain energy without considering about the environmental surroundings. Energy can be transferred wirelessly through many materials such as air, water, wood, rock, etc. WPT have been successfully integrated with a great number of research areas such as the induction heating [1], the bidirectional charging [2], electric vehicles (EVs) [3], novel magnetic structures [4], power-data-parallel transmission [5] and the coil design [6], etc.

In general, WPT can be separated into far-field and near-field WPT according to the transmission distance. The far-field WPT can be formed through energy carriers like the acoustic, the optical, and the microwave [7]. Lately, near-field plays an important role in EVs as well as consumer electronics such as smart phones, laptops, the intelligent watch and earphones. There are two dominant types for near-field WPT, namely, capacitive power transfer (CPT) and inductive power transfer (IPT) [8]. Usually, CPT makes use of the electric field from capacitive metal plate couplers, resulting in a superior capability to penetrate through metal materials that already exist in the transmission path [9, 10]. By contrast, IPT system generally takes advantage of high-frequency magnetic fields generated by coils. Coils can also be designed delicately for various charging purposes. In recent years, IPT becomes more and more mature thanks to latest developments in magnetic materials: LITZ wire, embedded controllers, and high-frequency power electronics [11, 12].

In this paper, only IPT is discussed since it tends to be more commercially attractive compared to CPT. One extremely popular charged objective is the battery since they are universally utilized in smart phones, EVs, unmanned aerial vehicles (UAVs), and many other consumer electronics. Moreover, high-quality batteries can also be integrated with microgrids [13] and alternative energy device such as solar photovoltaics [14]. Fig. 1 illustrates a typical charging profile. The charging process begins with the CC mode. As the voltage of the battery jumps to a stable stage, the charger goes into CV mode until the charging current declines to zero approximately [15]. However, during the period of battery charging, the equivalent resistance of a battery tends to be roughly varied from a few ohms to several hundred ohms [16]. Hence, the load-independent CC and CV are required to against the load variation. There are several methods to fulfill battery charging requirements with a WPT system. One popular means is to put a dc-dc converter to regulate the output value either at the source side or the load side [17]. However, complicated control methods are needed to control the bulky dc-dc converters [18].

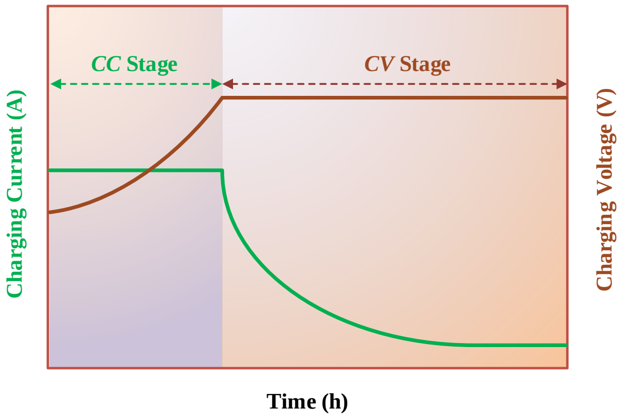

Fig. 1: The charging profile for the lithium-ion battery with CC and CV stages

Then, passive components are introduced to avoid complex control system and boost the simplicity. Well-organized compensation network can accomplish load-independent constant outputs including CC and CV, minimize VA rating and maximized power transfer capability, suppress bifurcation phenomenon and enhance the efficiency [19]. Basically, four compensation topologies including SS, SP, PS and PP are widely used in two-coil WPT [20] as shown in Fig. 2 (a)-(d). Recently, several high-order compensation topologies such as LCL and LCC become more and more interesting owing to their special capabilities.

As illustrated in Fig. 2 (e), LCL topologies are proposed due to several advantages. Firstly, the primary current is able to be regardless of the reflected impedance from the secondary side [21]. Secondly, LCL topologies are studied to improve misalignment tolerance and lower voltage stresses across compensation capacitors [22].

As demonstrated in Fig. 2 (f), LCC topology is composed of inductor-capacitor-capacitor structure both on the transmitter and receiver side. This topology can accomplish ZCS [23] and the inverter only requires to provide the active power with a primary-side load-independent current [24].

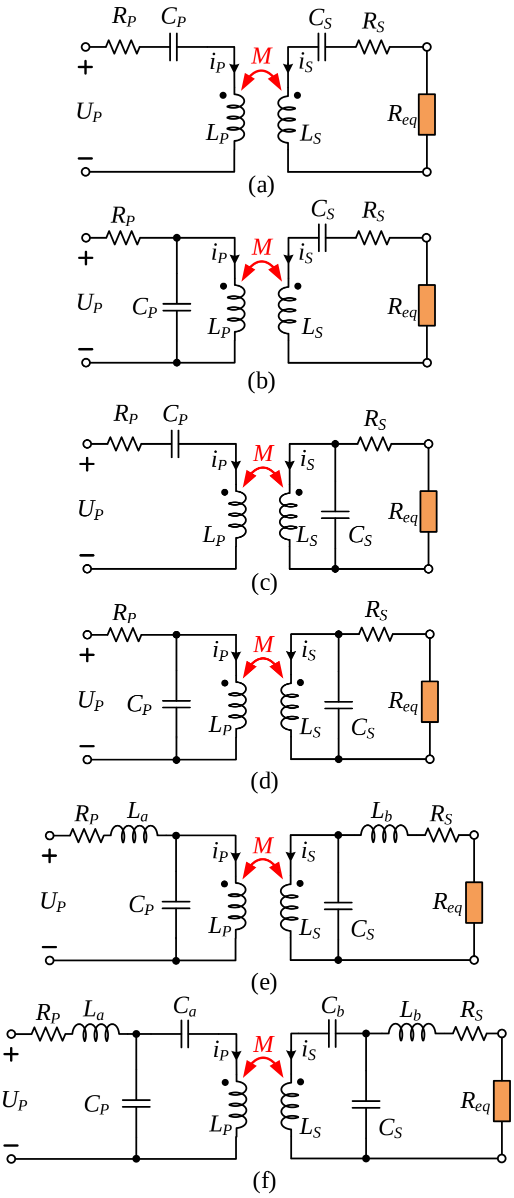

Fig. 2: Compensation topologies
(a) SS (b) PS (c) SP (d) PP (e) LCL (f) LCC

In addition, when it comes to existing wireless chargers, the communication from the receiver to the transmitter is often needed to build a closed-loop control to achieve the switch between CC and CV outputs. Nevertheless, wireless communication equipment tends to increase the system cost [25]. Furthermore, the wireless communication sometimes suffers from the interference created by the high-frequency magnetic field between the transmitter side and the receiver side. Especially, this may give rise to some problems like interruption or delay in some compact structures.

Therefore, a compact and switchable method is studied and built to resolve problems mentioned above. The key contributions are the following.

1) *Load-independent Outputs*: The load-independent CC and CV characteristics can be achieved by reconfiguring the circuit without any communication from the receiver to the transmitter. The system works in the CC mode within double LCL topology while CV mode within LCL-S topology.

2) *Simplicity and Reliability*: Only passive compensation topologies are used to regulate outputs. Without dc-dc converters, complicated control loops and corresponding interruption can be avoided. By eliminating the communication between the source and the load side, the proposed structure not only saves cost but also improves the robustness of the whole system.

3) *Compact Structure*: Without additional capacitors, pure LCL is more suitable for a compact structure. Besides, there is no need to put additional inductors far away from the main coupler to diminish unwanted couplings. Through inserting two ferrite cores, the unwanted couplings are greatly reduced while the major magnetic coupling from the transmitter and the receiver is enhanced. Moreover, the design of compensation networks can become more straightforward without considering unwanted couplings.

Nevertheless, the pure LCL structures give rise to the difficulty in designing magnetic couplers. Hence, finite element analysis (FEA) is used to well organize the proposed coupler. Detailed coupler design is demonstrated in section II. Section III provides fundamental analysis according to various circuits correspondingly. Section IV presents the experimental results with detailed hardware design and Section V concludes the whole paper.

II. COUPLER DESIGN

B. Coupler structure with detailed dimension

Fig. 3 depicts the proposed coupling structure including four spiral coils, i.e., L_a, L_P, L_S and L_b acting as the primary additional inductor, the transmitter coil, the receiver coil and the secondary additional inductor, respectively. For the compact purpose, the L_b and L_S are placed on upper surface and lower surface of ferrite core A, respectively. Likewise, L_P and L_a are installed on upper surface and lower surface of ferrite core B, respectively.

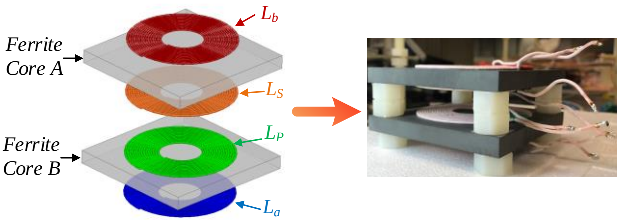

(a) (b)

Fig. 3: The expanded and manufactured view of proposed coupler structure (a) Expanded view (b) Manufactured view

As illustrated in Fig. 4, the shape and size of these four coils are almost identical. And they are all manufactured by high-quality 140-strand LITZ wire. The external diameter of coils is 80mm while the inner diameter is 30mm. Then, ferrite cores are purely square-shaped (100mm×100mm). The size of ferrite cores is designed to be slightly larger than the corresponding size of coils, which offers better magnetic shielding for unwanted couplings. The transmission distance between T_X and R_X is 20mm.

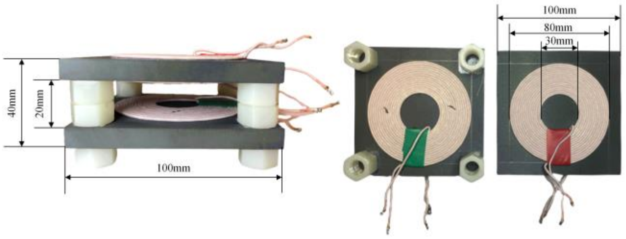

Fig. 4: Manufactured coupler structure with detailed dimension

B. Simulation results

The magnetic field distribution can be gained from finite element analysis software, which can be seen in Fig. 5. In this simulation, only the primary auxiliary coil L_a is excited to observe the magnetic field distribution directly. Fig. 5 depicts that the magnetic field generated from L_a mainly have the linkage with itself. That means the unwanted coupling from L_a is shielded by ferrite cores. There is no need to put L_a far away from the main coupling structure as conventional practice, contributing to a compact and concise configuration. Due to the symmetry of this design, the unwanted coupling from L_b is also greatly reduced from the same reason. Thus, only the major coupling k takes effects in this paper.

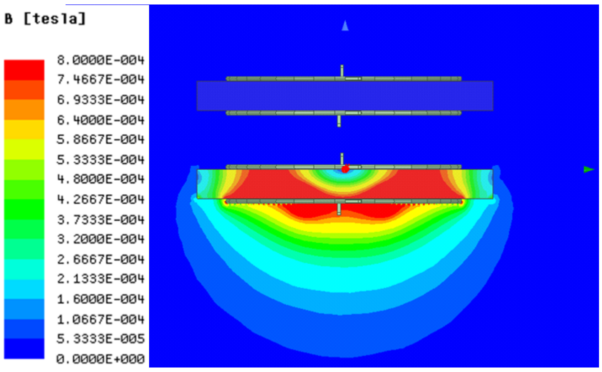

Fig. 5: A brief simulation result of the magnetic field

III. FUNDAMENTAL ANALYSIS

The entire scheme of the proposed WPT circuit model is demonstrated in Fig. 6. The primary DC voltage V_{dc} offered by DC power supply GP-1305DU from EZ Digital. The entire system is divided into two sides, i.e., the primary side through transmitter coil (T_X) and the secondary side through the receiver coil (R_X).

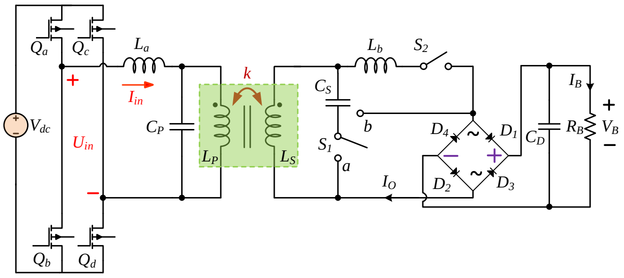

Fig. 6: The entire scheme of the proposed WPT circuit model

Ferrite cores made of material PC40 are used to enhance the magnetic coupling between T_X and R_X as a compact structure. The coupling coefficient k can be expressed as

$$k = \frac{M}{\sqrt{L_P \cdot L_S}} \tag{1}$$

where L_P and L_S are the self-inductances from T_X and R_X respectively and M is the mutual inductance between them. Due to the exist of ferrite cores, the unwanted coupling among L_a, L_b, R_X and T_X are all limited to an ignorable magnitude compared with the major coupling k between T_X and R_X. Next, V_B, I_B and R_B represent the voltage, current and the equivalent resistance of the battery, respectively.

The designed transmission distance is 2cm through the air from T_X to R_X. Then, the primary converter is a H-bridge inverter that is mainly composed of Q_a, Q_b, Q_c *and* Q_d. The secondary converter is a diode bridge rectifier (D_1, D_2, D_3, D_4 and C_D). The equivalent series resistances (ESRs) from the primary and secondary sides are neglected for simplification.

In terms of the inverter, its output voltage with 300ns dead time. Next, the root mean square (RMS) value of the β_{th} order harmonic component from the inverter output voltage u_{in} can be expressed as [26]

$$U_{in\_\beta} = \frac{2\sqrt{2}}{\beta\pi} V_{dc} (\beta = 1,3,5,7,9\ldots) \tag{2}$$

Because the high-order resonant circuit works as bandpass filters, higher order harmonics are mainly filtered out [26]. In this paper, only the fundamental component is taken into account for the sake of simplification and it can be written as [27].

$$\dot{U}_{in} = \frac{2\sqrt{2}V_{dc}}{\pi} \angle 0^{\circ} \tag{3}$$

As for the rectifier, the relationship between its input and output value can be shown as

$$U_O = \frac{2\sqrt{2}}{\pi} V_B \tag{4}$$

$$I_O = \frac{\pi}{2\sqrt{2}} I_B \tag{5}$$

R_{eq}, the equivalent load of the rectifier [28], can be gained as

$$R_{eq} = \frac{8}{\pi^2} R_B \tag{6}$$

Therefore, the rectifier part from Fig. 6 can be replaced by the equivalent load for simplification. The simplified diagram of the proposed WPT circuit model is illustrated in Fig. 7, where U_O and I_O are the input voltage and current value of the rectifier, respectively. Two switches, namely, S_1 and S_2 are used for the switching between CC and CV stages. S_1 works as a single-pole double-throw switch while S_2 acts as a single-pole single-throw switch. The configuration can be re-arranged through switches. Detailed information is shown as follows.

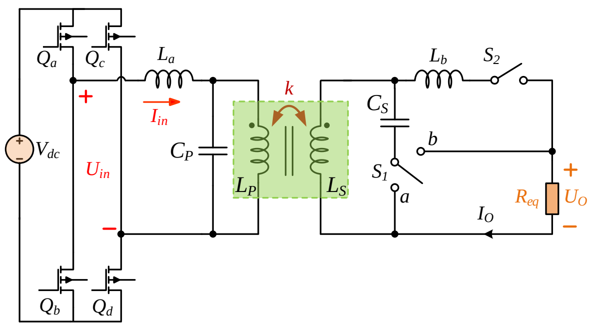

Fig. 7: The simplified diagram of the proposed WPT circuit model

A. The analysis of double LCL configuration for CC stage

As shown in Fig. 8, the circuit of the double LCL configuration is constructed when the switch S_1 is thrown to the terminal a as well as the S_2 is switched on. L_a, L_b, C_P and C_S are the auxiliary inductors and the resonant capacitors in the primary side and secondary side, respectively. For tuning the coils, the operating angular frequency of the inverter ω needs to meet the following equation:

$$\omega = \sqrt{\frac{1}{L_aC_P}} = \sqrt{\frac{1}{L_PC_P}} = \sqrt{\frac{1}{L_SC_S}} = \sqrt{\frac{1}{L_bC_S}} \tag{7}$$

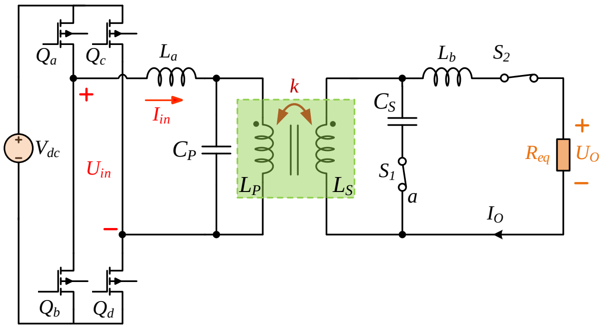

Fig. 8: The scheme of the double LCL WPT system

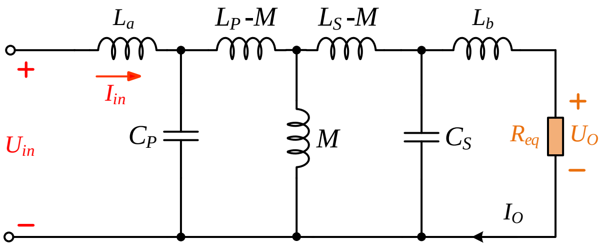

Fig. 9: The equivalent T-model of the double LCL WPT system

The equivalent T-model of the double LCL WPT system is demonstrated in Fig. 9. Through the conversion of the resonant circuits, the relationship between the input and output can be expressed as

$$\dot{I}_O = \frac{M}{j\omega L_S L_a}\dot{U}_{in} \tag{8}$$

Substituting (3) and (5) into (8), we can get

$$I_B = \frac{8M}{\pi^2 \omega L_S L_a} V_{dc} \tag{9}$$

Therefore, the current of the battery is independent of the load. A load-independent CC from the wireless charger can be gained through this double LCL configuration.

B. CV stage with LCL-S configuration

As shown in Fig. 10, the circuit of the double LCL configuration is constructed when the switch S_1 is thrown to the terminal b as well as the S_2 is switched off. L_a, L_b, C_P and C_S are the auxiliary inductors and the resonant capacitors in the primary side and secondary side, respectively. Similarly, ω should meet the following equation for tuning the coils.

$$\omega = \sqrt{\frac{1}{L_aC_P}} = \sqrt{\frac{1}{L_PC_P}} = \sqrt{\frac{1}{L_SC_S}} \tag{10}$$

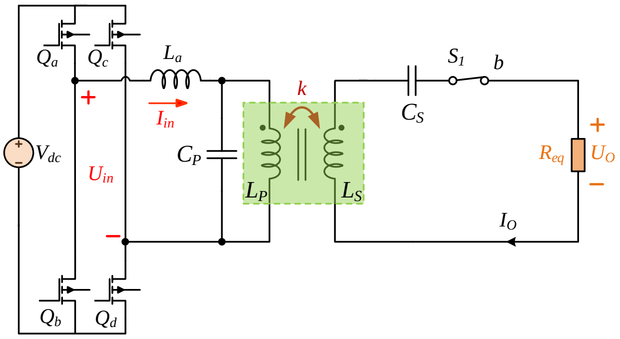

Fig. 10: The scheme of the LCL-S WPT system

The equivalent T-model of the LCL-S configuration is illustrated in Fig. 11. Through the conversion of the resonant circuits, the relationship between the input and output can be gained as

$$\dot{U}_O = \frac{M}{L_a}\dot{U}_{in} \tag{11}$$

Similarly, substituting (3) and (4) into (11), we can get

$$V_B = \frac{M}{L_a} V_{dc} \tag{12}$$

Thus, the voltage of the battery V_B is independent of the load. A load-independent CV from the wireless charger can be gained through this LCL-S configuration.

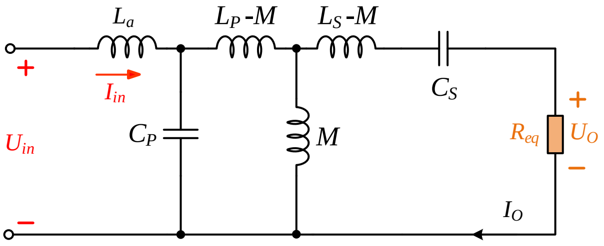

Fig. 11: The equivalent T-model of the LCL-S WPT system

IV. EXPERIMENTAL VERIFICATION

An experimental platform has been built up to verify the theoretical analysis as demonstrated in Fig. 12. The operating frequency from the inverter f is fixed as 200kHz. The battery is replaced by two resistive loads for simplification. There is a switch equipped with these two resistances for the dynamic response test when the load change happens. Experimental waveforms are directly gained and analysed from oscilloscope Tektronix MDO3024. The two output channels from power supply EZ Digital GP-1305DU are connected in series to power the inverter. The maximum output of this DC power supply device is approximately 60V. Two switches, namely, S_1 and S_2 are used to turn on/off specific loops. Measured parameters from this prototype can be found in Table. 1.

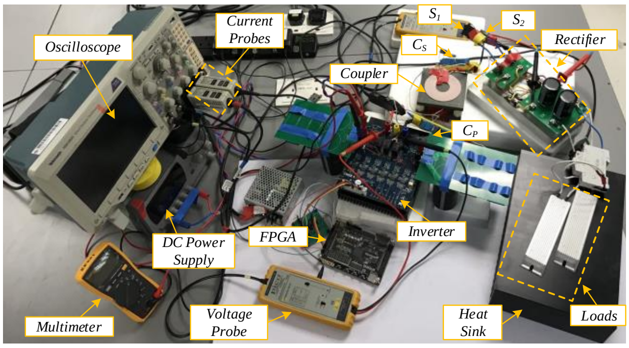

Fig. 12: The whole experimental prototype

Table 1: Measured parameters

L_a	L_P	L_S	L_b
23.79μH	24.02μH	23.85μH	24.01μH
M	C_P	C_S	f
12.32μH	26.03nF	26.19nF	200kHz

A. Experimental results of the double LCL configuration

Fig. 13 depicts the essential waveforms from the inverter and the output information at the load side. This inverter output current slightly lags the inverter output voltage, which reveals ZVS can be ensured through the double LCL configuration.

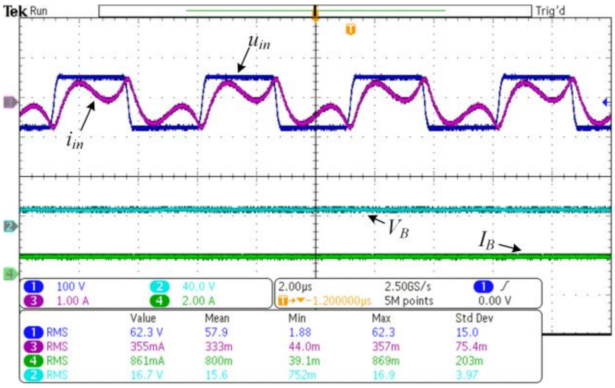

	Value	Mean	Min	Max	Std Dev
1 RMS	62.3 V	57.9	1.88	62.3	15.0
3 RMS	355mA	333m	44.0m	357m	75.4m
4 RMS	861mA	800m	39.1m	869m	203m
2 RMS	16.7 V	15.6	752m	16.9	3.97

Fig. 13: Essential waveforms from the inverter, the output voltage and current on the load in double LCL configuration

Fig. 14 illustrates the dynamic response during the process that the load is changed from 20Ω to 40Ω and then from 40Ω to 20Ω. The switching points are manifested by the dotted ellipse. The voltage variation is 16.8V that can be directly detected by the oscilloscope. However, the current on the load keeps at 880mA with slight overshoots as shown in Fig. 15, which verifies the CC characteristic from the double LCL configuration.

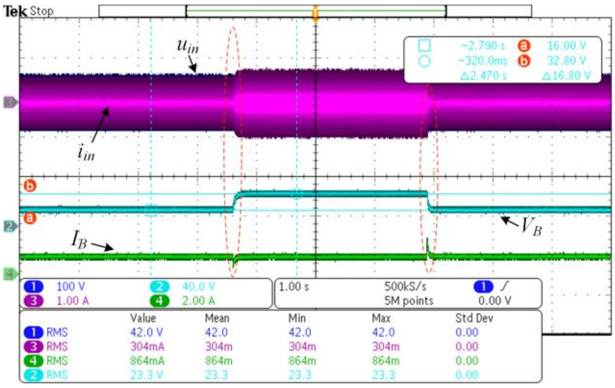

	Value	Mean	Min	Max	Std Dev
1 RMS	42.0 V	42.0	42.0	42.0	0.00
3 RMS	304mA	304m	304m	304m	0.00
4 RMS	864mA	864m	864m	864m	0.00
2 RMS	23.3 V	23.3	23.3	23.3	0.00

Fig. 14: Dynamic response with voltage data when the load changes from 20Ω to 40Ω and back to 20Ω in double LCL type

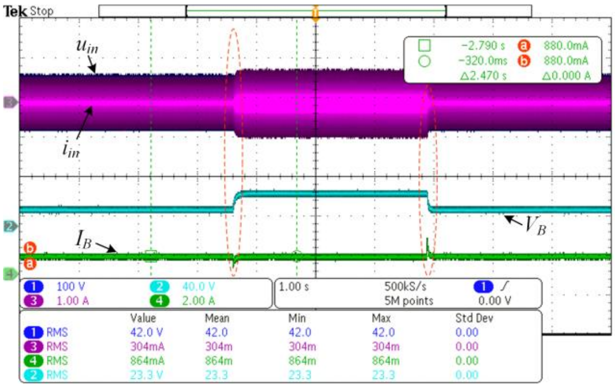

	Value	Mean	Min	Max	Std Dev
1 RMS	42.0 V	42.0	42.0	42.0	0.00
3 RMS	304mA	304m	304m	304m	0.00
4 RMS	864mA	864m	864m	864m	0.00
2 RMS	23.3 V	23.3	23.3	23.3	0.00

Fig. 15: Dynamic response with current data when the load changes from 20Ω to 40Ω and back to 20Ω in double LCL type

B. Experimental results of the LCL-S configuration

Fig. 16 describes the essential waveforms from the inverter and the output data from the load side. This inverter output current slightly lags the inverter output voltage, which shows this LCL-S configuration can achieve ZVS.

The dynamic response of LCL-S type can be observed from Fig. 17 during the process that the load is switched between 20Ω and 40Ω. The switching points are manifested by the dotted ellipse too. The change of load current is 800mA, which can be directly detected through the oscilloscope. However, the voltage on the load keeps stable at 30.4V as illustrated in Fig. 18 when load variation happens, which validates the CV characteristic from the LCL-S configuration.

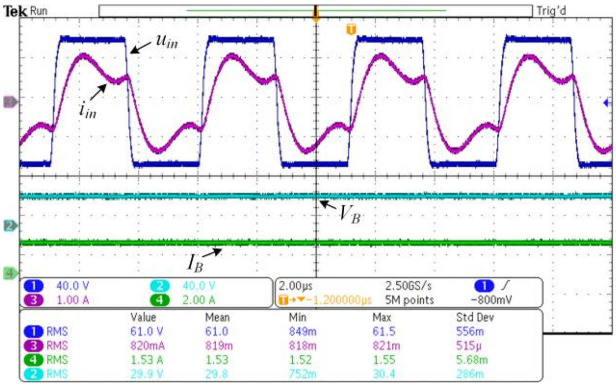

	Value	Mean	Min	Max	Std Dev
1 RMS	61.0 V	61.0	849m	61.5	556m
3 RMS	820mA	819m	818m	821m	515μ
4 RMS	1.53 A	1.53	1.52	1.55	5.68m
2 RMS	29.9 V	29.8	752m	30.4	286m

Fig. 16: Essential waveforms from the inverter, the output voltage and current on the load in LCL-S type

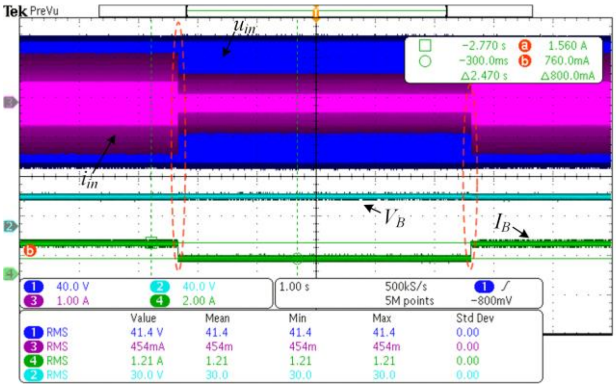

	Value	Mean	Min	Max	Std Dev
1 RMS	41.4 V	41.4	41.4	41.4	0.00
3 RMS	454mA	454m	454m	454m	0.00
4 RMS	1.21 A	1.21	1.21	1.21	0.00
2 RMS	30.0 V	30.0	30.0	30.0	0.00

Fig. 17: Dynamic response with current data when the load changes from 20Ω to 40Ω and back to 20Ω in LCL-S type

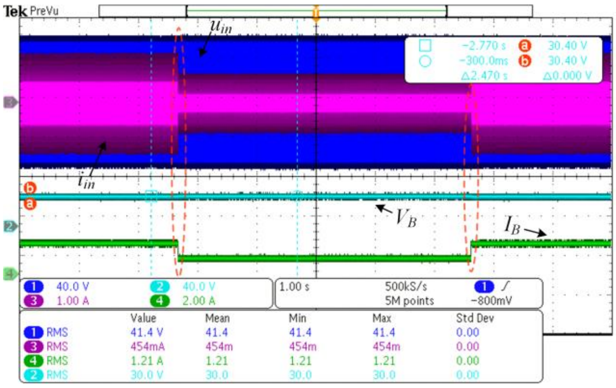

	Value	Mean	Min	Max	Std Dev
1 RMS	41.4 V	41.4	41.4	41.4	0.00
3 RMS	454mA	454m	454m	454m	0.00
4 RMS	1.21 A	1.21	1.21	1.21	0.00
2 RMS	30.0 V	30.0	30.0	30.0	0.00

Fig. 18: Dynamic response with voltage data when the load changes from 20Ω to 40Ω and back to 20Ω in LCL-S type

V. CONCLUSION

A compact design for a switchable wireless charger is investigated in this paper. Special magnetic coupler equipped with ferrite cores are proposed to enhance the major coupling between T_X and R_X as well as to reduce the unwanted cross-couplings simultaneously. By doing this, the coupling coefficient between T_X and R_X is improved and the compensation networks can be designed straightforward. Key characteristics such as ZVS, load-independent CC and CV are demonstrated through essential waveforms. In particular, the fundamental analysis, the mathematical derivation, detailed circuit analysis, compensation network designs are all discussed and studied. An experimental prototype is built to evaluate the performance and related test results successfully show the agreement with the analysis. The design in this paper can be adjusted in size to meet the needs of different IPT systems for wirelessly charging smart phones, UAVs, or EVs.

REFERENCES

[1] L. Meng and K. W. E. Cheng, "Wireless power transfer technology for electric iron based on multi-coils induction heating design," *IET Power Electronics,* vol. 12, no. 10, pp. 2566-2577, 2019.

[2] Y. C. Fong and K. W. E. Cheng, "A switched-capacitor step-up inverter for bidirectional wireless charging applications in electric microcar," in *2017 7th International Conference on Power Electronics Systems and Applications - Smart Mobility, Power Transfer & Security (PESA)*, 12-14 Dec. 2017 2017, pp. 1-6,

[3] K. W. K. Chen and K. W. E. Cheng, "Review of magnetic resonance technology, recent research trends and issues in EV wireless charging," in *The 11th IET International Conference on Advances in Power System Control, Operation and Management (APSCOM 2018)*, 11-15 Nov. 2018 2018, pp. 1-7,

[4] M. Chen, E. K. Cheng, and J. Hu, "Near Field Wireless Power Transfer for Multiple Receivers by Using a Novel Magnetic Core Structure," in *2018 IEEE Energy Conversion Congress and Exposition (ECCE)*, 23-27 Sept. 2018 2018, pp. 1190-1195,

[5] X. Li, J. Hu, Y. Li, H. Wang, M. Liu, and P. Deng, "A Decoupled Power and Data-Parallel Transmission Method With Four-Quadrant Misalignment Tolerance for Wireless Power Transfer Systems," *IEEE Transactions on Power Electronics,* vol. 34, no. 12, pp. 11531-11535, 2019.

[6] Y. Li *et al.*, "A New Coil Structure and Its Optimization Design With Constant Output Voltage and Constant Output Current for Electric Vehicle Dynamic Wireless Charging," *IEEE Transactions on Industrial Informatics,* vol. 15, no. 9, pp. 5244-5256, 2019.

[7] Z. Zhang, H. Pang, A. Georgiadis, and C. Cecati, "Wireless Power Transfer—An Overview," *IEEE Transactions on Industrial Electronics,* vol. 66, no. 2, pp. 1044-1058, 2019.

[8] X. Mou and H. Sun, "Wireless Power Transfer: Survey and Roadmap," in *2015 IEEE 81st Vehicular Technology Conference (VTC Spring)*, 11-14 May 2015 2015, pp. 1-5,

[9] L. Huang, A. P. Hu, A. K. Swain, and Y. Su, "Z-Impedance Compensation for Wireless Power Transfer Based on Electric Field," *IEEE Transactions on Power Electronics,* vol. 31, no. 11, pp. 7556-7563, 2016.

[10] Y. Su, S. Xie, A. P. Hu, C. Tang, W. Zhou, and L. Huang, "Capacitive Power Transfer System With a Mixed-Resonant Topology for Constant-Current Multiple-Pickup Applications," *IEEE Transactions on Power Electronics,* vol. 32, no. 11, pp. 8778-8786, 2017.

[11] G. A. Covic and J. T. Boys, "Modern Trends in Inductive Power Transfer for Transportation Applications," *IEEE Journal of Emerging and Selected Topics in Power Electronics,* vol. 1, no. 1, pp. 28-41, 2013.

[12] G. A. Covic and J. T. Boys, "Inductive Power Transfer," *Proceedings of the IEEE,* vol. 101, no. 6, pp. 1276-1289, 2013.

[13] J. Hu, Y. Xu, K. W. Cheng, and J. M. Guerrero, "A model predictive control strategy of PV-Battery microgrid under variable power generations and load conditions," *APPL ENERG,* vol. 221, pp. 195-203, 2018.

[14] Y. Shan, J. Hu, K. W. Cheng, and M. Liu, "A Universal

Model Predictive Control for Practical AC Microgrids with PVs and Battery Energy Storage Systems," in *2018 IEEE Energy Conversion Congress and Exposition (ECCE)*, 23-27 Sept. 2018 2018, pp. 6257-6262,

[15] X. Qu, H. Han, S. Wong, C. K. Tse, and W. Chen, "Hybrid IPT Topologies With Constant Current or Constant Voltage Output for Battery Charging Applications," *IEEE Transactions on Power Electronics,* vol. 30, no. 11, pp. 6329-6337, 2015.

[16] G. Buja, M. Bertoluzzo, and K. N. Mude, "Design and Experimentation of WPT Charger for Electric City Car," *IEEE Transactions on Industrial Electronics,* vol. 62, no. 12, pp. 7436-7447, 2015.

[17] Y. Li, Y. Sun, and X. Dai, "/spl mu/-Synthesis for Frequency Uncertainty of the ICPT System," *IEEE Transactions on Industrial Electronics,* vol. 60, no. 1, pp. 291-300, 2013.

[18] C. Xia, W. Wang, G. Chen, X. Wu, S. Zhou, and Y. Sun, "Robust Control for the Relay ICPT System Under External Disturbance and Parametric Uncertainty," *IEEE Transactions on Control Systems Technology,* vol. 25, no. 6, pp. 2168-2175, 2017.

[19] W. Zhang and C. C. Mi, "Compensation Topologies of High-Power Wireless Power Transfer Systems," *IEEE Transactions on Vehicular Technology,* vol. 65, no. 6, pp. 4768-4778, 2016.

[20] Y. Wang, H. Wang, T. Liang, X. Zhang, D. Xu, and L. Cai, "Analysis and design of an LCC/S compensated resonant converter for inductively coupled power transfer," in *2017 IEEE Transportation Electrification Conference and Expo, Asia-Pacific (ITEC Asia-Pacific)*, 7-10 Aug. 2017 2017, pp. 1-5,

[21] H. Hao, G. A. Covic, and J. T. Boys, "An Approximate Dynamic Model of LCL- T-Based Inductive Power Transfer Power Supplies," *IEEE Transactions on Power Electronics,* vol. 29, no. 10, pp. 5554-5567, 2014.

[22] N. A. Keeling, G. A. Covic, and J. T. Boys, "A Unity-Power-Factor IPT Pickup for High-Power Applications," *IEEE Transactions on Industrial Electronics,* vol. 57, no. 2, pp. 744-751, 2010.

[23] Z. Pantic, S. Bai, and S. M. Lukic, "ZCS LCC-Compensated Resonant Inverter for Inductive-Power-Transfer Application," *IEEE Transactions on Industrial Electronics,* vol. 58, no. 8, pp. 3500-3510, 2011.

[24] S. Li, W. Li, J. Deng, T. D. Nguyen, and C. C. Mi, "A Double-Sided LCC Compensation Network and Its Tuning Method for Wireless Power Transfer," *IEEE Transactions on Vehicular Technology,* vol. 64, no. 6, pp. 2261-2273, 2015.

[25] Y. Li *et al.*, "Reconfigurable Intermediate Resonant Circuit Based WPT System With Load-Independent Constant Output Current and Voltage for Charging Battery," *IEEE Transactions on Power Electronics,* vol. 34, no. 3, pp. 1988-1992, 2019.

[26] Y. Li *et al.*, "Analysis, Design, and Experimental Verification of a Mixed High-Order Compensations-Based WPT System with Constant Current Outputs for Driving Multistring LEDs," *IEEE Transactions on Industrial Electronics,* vol. 67, no. 1, pp. 203-213, 2020.

[27] H. Cai, L. Shi, and Y. Li, "Harmonic-Based Phase-Shifted Control of Inductively Coupled Power Transfer," *IEEE Transactions on Power Electronics,* vol. 29, no. 2, pp. 594-602, 2014.

[28] Y. Li, Q. Xu, T. Lin, J. Hu, Z. He, and R. Mai, "Analysis and Design of Load-Independent Output Current or Output Voltage of a Three-Coil Wireless Power Transfer System," *IEEE Transactions on Transportation Electrification,* vol. 4, no. 2, pp. 364-375, 2018.

Development of Front-End Monitoring of Mutual Coupling and Load Conditions in Wireless Power Transfer Systems

Yun Yang[a]
[a]Department of Electrical Engineering, The Hong Kong Polytechnic University, Hong Kong, China
Email: yun1989.yang@polyu.edu.hk

Abstract–A conventional series-series (SS)-compensated wireless power transfer (WPT) system generally comprises a DC-DC regulator at the user-end for the battery charging, which will deteriorate the dynamic response and efficiency of the system. To address this issue, maximum efficiency tracking control methods based on direct communication feedback signals from the receiver to the transmitter are designed to estimate the coupling coefficient and load conditions. However, wireless communication systems can increase both cost and volume of the WPT system. Therefore, several primary-side monitoring strategies are proposed in recent years. This paper covers main content of the tutorial that is presented in 8th PESA, in which the development of front-end monitoring strategies from the Wireless Power Research Group of the University of Hong Kong are described.

***Keywords*-Front-end monitoring strategies, series-series (SS)-compensated wireless power transfer (WPT), coupling coefficient, load condition.**

I. INTRODUCTION

EARLY investigations of non-radiative WPT via near-field magnetically coupled resonators can be traced back to the late 19th century by Nicola Tesla [1]. Based on his inventions, non-radiative WPT are applied in transcutaneous systems, inductive power pick-up systems and portable electronics systems in the 1970s, 1990s and 2000s, respectively [2-4]. The dawn of mobile phones in the 1990s accelerates the development of non-radiative wireless power transfer (WPT) and triggers the foundation of Wireless Power Consortium (WPC) [5]. The eight founders of WPC made an agreement to adopt inductive coupling in the world first wireless standard “Qi”. By far, more than 3700 “Qi-certified” products have been registered with WPC by over companies worldwide [6]. Although “Qi” is the earliest published specification for near-field WPT, it is not the only standard. The A4WP proposed by AirFuel Alliance (AFA) [7] and SAE TIR J2954 launched by Society of Automotive Engineers (SAE) [8] are the two alternative industrial guidelines that primarily focus on multiple charging devices and high-power applications in light-duty electric and plug-in electric vehicles, respectively. The key features of the three industrial guidelines are quite different. However, the three guidelines have a common feature that is the adoption of Tesla’s principle to compensate the leakage inductance by various compensation topologies [9]. Among them, the SS-compensation is most widely adopted [10].

In practical SS-compensated WPT systems, communication devices are often adopted to ensure reliable and high-efficiency operations by delivering feedback signals from the user-ends to the front-ends. However, the communication devices quite annoy manufactures by enhancing complexity, bringing additional costs, and deteriorating dynamic performance of WPT systems [11-13]. More importantly, an exclusive communication standard may be adopted, which is undesirable by most manufactures. To reduce this anxiety, front-end monitoring strategies are developed by the research groups worldwide [14-23]. Apart from the eliminations of communication devices, the front-end monitoring strategies for the parameters, such as mutual inductances and load resistances, can also improve the dynamic performance and overall transfer efficiency when the operation conditions vary [24, 25].

This paper focus on various front-end monitoring strategies that has been developed by the Wireless Power Research Group of the University of Hong Kong so far. The roadmap of the front-end monitoring strategies is presented in the tutorial session “Development of Front-end Monitoring of Mutual Coupling and Load Conditions in Wireless Power Transfer Systems” of the 8th PESA. The early monitoring method is designed based on the primary-side measurements to solely estimate the load impedance of an SS-compensated WPT system [18]. However, only one load impedance can be estimated by this monitoring method and mutual inductances are required to be preliminarily known. To this end, an advanced monitoring method is presented for monitoring two loads in a four-coil SS-compensated WPT system using only the primary-side measurements [19]. Besides, research is extended to exhibit that both the load resistance and the mutual inductance can be monitored [20]. Simplified estimation equations, which can be easily implemented using inexpensive digital controllers, are further developed in [21]. Nevertheless, the parameter deviations will affect the accuracies of the monitoring strategies in [20] and [21]. To address this critical issue, a two-layer adaptive Differential Evolution (ADE) algorithm is proposed to monitor not only the mutual inductances and load resistances, but also the parameters of the receivers [22]. These “model-based” monitoring methods need mathematical calculations based on the equivalent circuit at fundamental resonant frequency. Alternatively, a fast “hardware-based” monitoring strategy is also proposed for the estimations of mutual inductances [23]. This paper reviews both the “model-based” and “hardware-based” monitoring methods for SS-compensated WPT systems in [18-23]. Conclusions and future works are also discussed.

II. “MODEL-BASED” MONITORING STRATEGIES

A. *Single Load Monitoring*

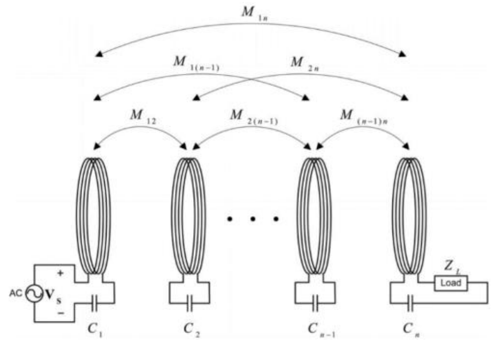

Fig. 1. Schematic of an *n*-coil wireless power transfer system with one load [18].

For an *n*-coil SS-compensated WPT system with only one load, as shown in Fig. 1, based on the Kirchhoff's voltage law, the system can be described in a general matrix as

$$\begin{bmatrix} V_s \\ 0 \\ \vdots \\ 0 \\ 0 \end{bmatrix} = \begin{bmatrix} Z_1 & j\omega M_{12} & \cdots & j\omega M_{1(n-1)} & j\omega M_{1n} \\ j\omega M_{12} & Z_2 & \cdots & j\omega M_{2(n-1)} & j\omega M_{2n} \\ \vdots & \vdots & \ddots & \vdots & \vdots \\ j\omega M_{1(n-1)} & j\omega M_{2(n-1)} & \cdots & Z_{n-1} & j\omega M_{(n-1)n} \\ j\omega M_{1n} & j\omega M_{2n} & \cdots & j\omega M_{(n-1)n} & Z_n + Z_L \end{bmatrix} \times \begin{bmatrix} \mathbf{I_1} \\ \mathbf{I_2} \\ \vdots \\ \mathbf{I_{n-1}} \\ \mathbf{I_n} \end{bmatrix} \tag{1}$$

where V_s is the input AC input voltage of the transmitter. Z_1, Z_2, …, Z_{n-1}, Z_n are the equivalent impedances of the resonators. Z_L is the load impedance. M_{ij} indicates the mutual inductance between the *i*-th coil and the *j*-th coil (i.e., $M_{ij}=M_{ji}$). In the system model (1), the coils are coupled to each other while the load is not coupled to any one of the coils. The load can be either linear or nonlinear load. The load impedance Z_L can be derived based on the system model as

$$Z_L = \frac{D_n}{D_{n-1}} \tag{2}$$

where $D_{n-1} = \begin{vmatrix} j\omega M_{12} & j\omega M_{13} & \cdots & \mathbf{V_s} - Z_1\mathbf{I_1} & 0 \\ Z_2 & j\omega M_{23} & \cdots & -j\omega M_{12}\mathbf{I_1} & 0 \\ \vdots & \vdots & \ddots & \vdots & \vdots \\ j\omega M_{2(n-1)} & j\omega M_{3(n-1)} & \cdots & -j\omega M_{1(n-1)n}\mathbf{I_1} & 0 \\ j\omega M_{2n} & j\omega M_{3n} & \cdots & -j\omega M_{1n}\mathbf{I_1} & 1 \end{vmatrix}$

and $D_n = \begin{vmatrix} j\omega M_{12} & j\omega M_{13} & \cdots & j\omega M_{1n} & \mathbf{V_s} - Z_1\mathbf{I_1} \\ Z_2 & j\omega M_{23} & \cdots & j\omega M_{2n} & -j\omega M_{12}\mathbf{I_1} \\ \vdots & \vdots & \ddots & \vdots & \vdots \\ j\omega M_{2(n-1)} & j\omega M_{3(n-1)} & \cdots & j\omega M_{(n-1)n} & -j\omega M_{1(n-1)n}\mathbf{I_1} \\ j\omega M_{2n} & j\omega M_{3n} & \cdots & Z_n & -j\omega M_{1n}\mathbf{I_1} \end{vmatrix}$.

The schematic diagram of the setup and results in [18] are shown in Figs. 2 and 3, respectively. The load resistances are accurately monitored.

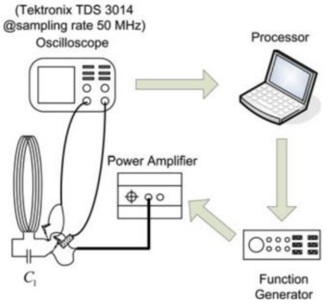

Fig. 2. Schematic diagram of the practical setup in [18].

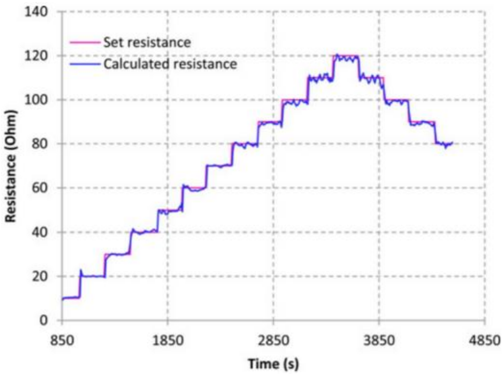

Fig. 3. Practical set resistance and the monitored resistance in [18].

B. Two Loads Monitoring

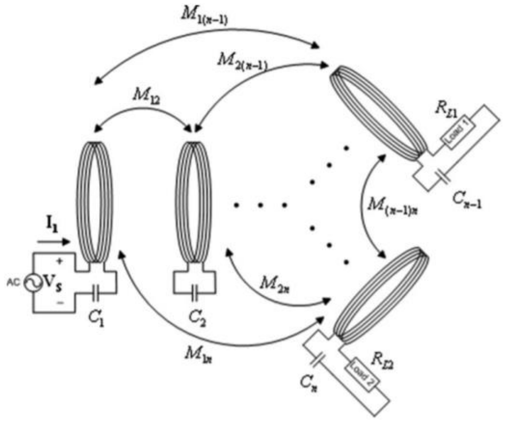

Fig. 4. Schematic of an *n*-coil wireless power transfer system with two loads [19].

For an *n*-coil SS-compensated WPT system with two loads, as shown in Fig. 4, based on the Kirchhoff's voltage law, the system can be described in a general matrix as

$$\begin{bmatrix} V_s \\ 0 \\ \vdots \\ 0 \\ 0 \end{bmatrix} = \begin{bmatrix} Z_1 & j\omega M_{12} & \cdots & j\omega M_{1(n-1)} & j\omega M_{1n} \\ j\omega M_{12} & Z_2 & \cdots & j\omega M_{2(n-1)} & j\omega M_{2n} \\ \vdots & \vdots & \ddots & \vdots & \vdots \\ j\omega M_{1(n-1)} & j\omega M_{2(n-1)} & \cdots & Z_{n-1} + R_{L1} & j\omega M_{(n-1)n} \\ j\omega M_{1n} & j\omega M_{2n} & \cdots & j\omega M_{(n-1)n} & Z_n + R_{L2} \end{bmatrix} \times \begin{bmatrix} \mathbf{I_1} \\ \mathbf{I_2} \\ \vdots \\ \mathbf{I_{n-1}} \\ \mathbf{I_n} \end{bmatrix} \tag{3}$$

where the two loads are purely resistive. By assuming R_{L1} is a known parameter, the system model in (3) can be rewritten as

$$\begin{bmatrix} \mathbf{I_2} \\ \mathbf{I_3} \\ \vdots \\ \mathbf{I_n} \\ R_{L2}\mathbf{I_n} \end{bmatrix} = \mathbf{P} \times \begin{bmatrix} \mathbf{V_s} - Z_1\mathbf{I_1} \\ -j\omega M_{12}\mathbf{I_1} \\ \vdots \\ -j\omega M_{1(n-1)n}\mathbf{I_1} - R_{L1}\mathbf{I_{n-1}} \\ -j\omega M_{1n}\mathbf{I_1} \end{bmatrix} \tag{4}$$

where $\mathbf{P} = \begin{bmatrix} j\omega M_{12} & j\omega M_{13} & \cdots & j\omega M_{1n} & 0 \\ Z_2 & j\omega M_{23} & \cdots & j\omega M_{2n} & 0 \\ \vdots & \vdots & \ddots & \vdots & \vdots \\ j\omega M_{2(n-1)} & j\omega M_{3(n-1)} & \cdots & j\omega M_{(n-1)n} & 0 \\ j\omega M_{2n} & j\omega M_{3n} & \cdots & Z_n & 1 \end{bmatrix}^{-1}$.

The last three equations in (4) are

$$\mathbf{I_{n-1}} = a + bR_{L1}\mathbf{I_{n-1}} \tag{5.1}$$

$$\mathbf{I_n} = c + dR_{L1}\mathbf{I_{n-1}} \tag{5.2}$$

$$R_{L2}\mathbf{I_n} = e + fR_{L1}\mathbf{I_{n-1}} \tag{5.3}$$

where

$$\begin{cases} a = \mathbf{P_{n-2}V} \\ b = -p_{(n-2)(n-1)} \\ c = \mathbf{P_{n-1}V} \\ d = -p_{(n-1)(n-1)} \\ e = \mathbf{P_n V} \\ f = -p_{n(n-1)} \end{cases}$$

$$\mathbf{V}=\begin{bmatrix}\mathbf{V_S}-Z_1\mathbf{I_1}\\ -j\omega M_{12}\mathbf{I_1}\\ \vdots\\ -j\omega M_{1(n-1)}\mathbf{I_1}\\ -j\omega M_{1n}\mathbf{I_1}\end{bmatrix}$$

Based on (5.1)~(5.3), the relationships between the R_{L1} and R_{L2} can be derived as

$$AR_{L1}R_{L2}+BR_{L1}+CR_{L2}+D=0 \qquad (6)$$

where

$$\begin{cases}A=ad-bc=\alpha_A+j\beta_A\\ B=be-af=\alpha_B+j\beta_B\\ C=c=\alpha_C+j\beta_C\\ D=-e=\alpha_D+j\beta_D\end{cases}$$

By reorganizing the real and imaginary terms and eliminating the nonlinear term $R_{L1}R_{L2}$, the equation (6) can be further derived as

$$(\alpha_B\beta_A-\alpha_A\beta_B)R_{L1}+(\alpha_C\beta_A-\alpha_A\beta_C)R_{L2}=\alpha_A\beta_D-\alpha_D\beta_A \quad (7)$$

Apparently, only two sets of **Vs** and **I₁** measurements at two different frequencies can be used to calculate the two load resistances in theory. Simulation results in Fig. 5 show that one intersection point of R_{L1} and R_{L2} can be plotted at various operating frequencies under ideal conditions.

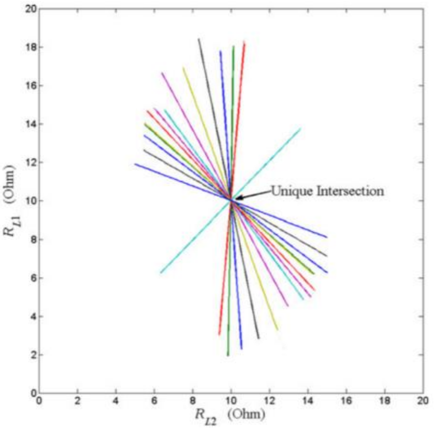

Fig. 5. One intersection points of the two loads at various operating frequencies under ideal conditions [19].

Experiments are conducted on a four-coil SS-compensated WPT system with two loads, as shown in Fig. 6. Based on 20 different frequency sweeping (20 equations are adopted), the two load resistances are monitored with high accuracy, as shown in Fig. 7.

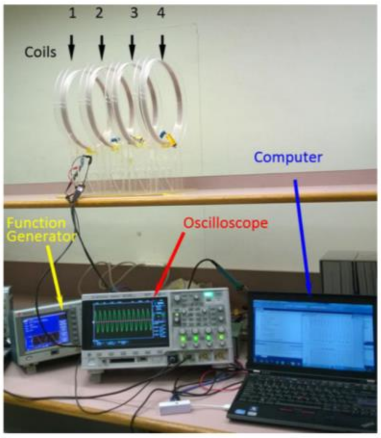

Fig. 6. Experimental setup in [19].

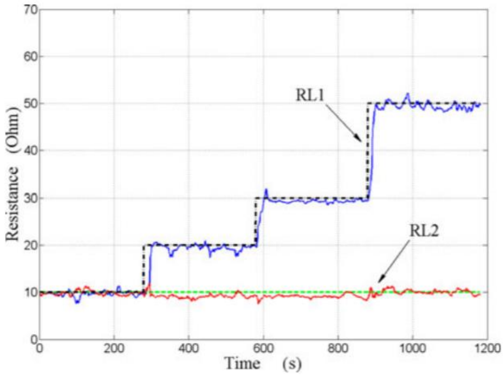

Fig. 7. Experimental results in [19].

C. *Mutual Inductance and Single Load Monitoring*

The system model in the frequency domain can be derived as

$$\begin{bmatrix}\mathbf{V_s}\\0\end{bmatrix}=\begin{bmatrix}Z_1 & j\omega M_{12}\\ j\omega M_{12} & Z_2+R_L\end{bmatrix}\begin{bmatrix}\mathbf{I_1}\\ \mathbf{I_2}\end{bmatrix} \qquad (8)$$

Based on (8),

$$R_L=\frac{R_L\mathbf{I_2}}{\mathbf{I_2}}=\frac{(\omega M_{12})^2+Z_1Z_2-Z_2Z_{\text{in}}}{Z_{\text{in}}-Z_1}=\frac{(\omega M_{12})^2}{Z_{\text{in}}-Z_1}-Z_2 \qquad (9)$$

where $Z_{\text{in}}=\frac{V_S}{I_1}\angle\varphi$. For purely resistive loads, the imaginary part is zero. Then, the mutual inductance and load resistance can be estimated based on

$$M_{12}=\sqrt{\frac{\omega L_2-\frac{1}{\omega C_2}}{\omega^2\mathbf{Im}(Z_{\text{in}}-Z_1)^{-1}}} \qquad (10)$$

$$R_L=\frac{\omega L_2-\frac{1}{\omega C_2}}{(Z_{\text{in}}-Z_1)\mathbf{Im}(Z_{\text{in}}-Z_1)^{-1}}-Z_2 \qquad (11)$$

Experiments are conducted on the coils with different positions in [20]. The load resistance is 25.8 Ω while the mutual inductances are changed from (a) the initial position about 23 μH to (b) the axial separation about 16 μH to (c) the lateral misalignment about 21 μH to (d) the angular misalignment about 16.7 μH. Obviously, the proposed monitoring strategy is accurate for both load resistance and mutual inductance.

(a) (b) (c) (d)

Fig. 8. Different coil positions in [20].

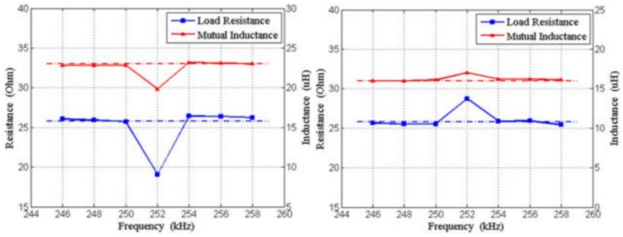

(a) (b)

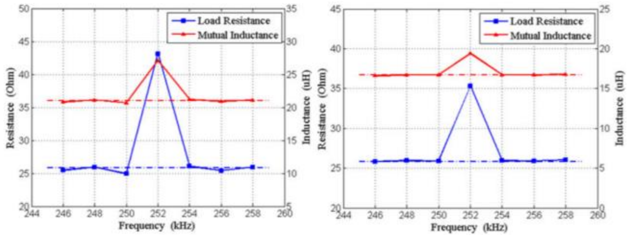

(c) (d)

Fig. 9. Monitoring results for the load resistance and mutual inductances in [20].

The load monitoring equation is further simplified in [21], which can be implemented using inexpensive digital controllers. Besides, the monitoring errors caused by the parameter drifts and measurement errors are mitigated as compared to the conventional monitoring strategy. The load monitoring equation in [21] is

$$R_L = \frac{Z_s V_{in} \cos\theta - R_p Z_s I_p}{V_{in} \sin\theta + Z_p I_p} - R_s \quad (a \neq 1) \tag{12}$$

The schematic diagram of the monitoring strategy is shown in Fig. 10.

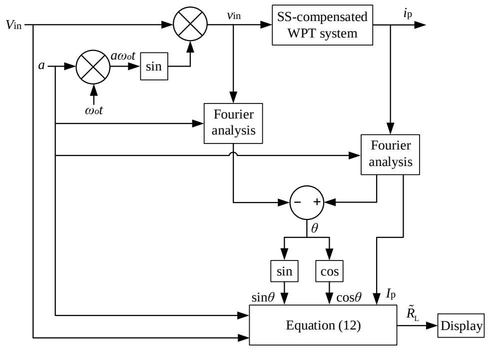

Fig. 10. Schematic diagram of the load monitoring strategy in [21].

The simulation results with the input voltage of 61.12 V, load resistances of 10 Ω and 50 Ω, and different mutual inductances are shown in Fig. 11.

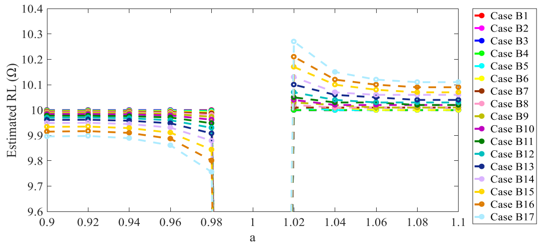

(a) V_{in}=61.12 V and R_L=10 Ω

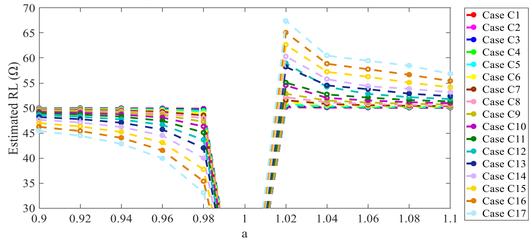

(b) V_{in}=61.12 V and R_L=50 Ω

Fig. 11. Simulation results in [21].

D. Heuristic Algorithm Method

The pioneers have developed several different monitoring strategies to effectively monitor one or two loads and mutual inductances of WPT systems with SS compensations [18-21]. However, these methods are invalidated for WPT systems with multiple loads and unknown parameters of the receivers. To bridge the research gaps, heuristic algorithms are adopted to monitor not only the load resistances and mutual inductances, but also the parameters of the receivers [22]. Details of the analysis and results can be found in [22].

III. “HARDWARE-BASED” MONITORING STRATEGY

For the “model-based” methods, the parameters of the transmitter and receiver resonators need to be preliminarily known. However, the sensitivities of the parasitic parameters are high in some WPT systems. Besides, for those heuristic algorithm methods, the total monitoring time is quite long and the algorithms are too complicated to be implemented using inexpensive digital controllers. To this end, a “hardware-based” monitoring method is proposed in [23]. However, the “hardware-based” monitoring method is only validated for the systems with active rectifiers (some commonly used active rectifiers as shown in Fig. 12). The “hardware-based” monitoring strategy is conducted by controlling the outputs of active rectifiers in short circuit. Therefore, the proposed monitoring strategy can be adopted for a WPT system with different loads. Details of the “hardware-based” method can be found in [23].

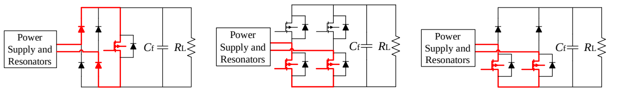

(a) (b) (c)

Fig. 12. Some examples of active rectifiers in SS-compensated WPT systems.

VI. CONCLUSIONS AND FUTURE WORKS

In this paper, the front-end monitoring strategies, including four “model-based” methods and one “hardware-based” method, that have been developed by the Wireless Power Research Group of the University of Hong Kong is presented. Based on the initial work of monitoring a single load in WPT systems with SS compensations, the researchers improve the strategy to monitor the SS-compensated WPT systems with two loads. On the other hand, the monitoring strategy is extended to monitor the load and the mutual inductance simultaneously for a two-stage SS-compensated WPT system. Later on, a simplified load monitoring strategy is further proposed. However, these monitoring methods are designed based on a WPT system with preliminary known parameters. To address the issue of WPT systems with uncertain parameters of the receivers, heuristic algorithm methods are further developed. Nevertheless, these “model-based” methods suffer from either high sensitivity issues of the parasitic parameters or long monitoring time. To this end, a “hardware-based” monitoring strategy is recently proposed to achieve both accurate and fast monitoring at the front-end. However, the “hardware-based” method is only validated for SS-compensated WPT systems with active rectifiers.

In the future works, front-end monitoring based on the dynamic models of the WPT systems maybe a promising strategy, particularly for the moving wireless charging of EV. Besides, front-end monitoring for the WPT systems with LCL-S or LCC-S compensation maybe another research trend, since the advantages of these two compensation schemes over the conventional SS compensation in the applications of EV charging have been demonstrated. Moreover, the Artificial Intelligence (AI) maybe used to achieve fast online monitoring of mutual coupling and load conditions by considering the parasitic parameters in the resonators and power converters.

REFERENCES

[1] N. Tesla, *On Light and Other High Frequency Phenomena*, Philadelphia: Lecture Delivered before the Franklin Institute, Feb. 1893.

[2] J. C. Schuder, I. H. Gold, and H. E. Stephenson, Jr., “An inductively coupled RF system for the transmission of 1 kW of power through the skin,” *IEEE Trans. Biomed. Eng.*, vol. BME-18, no. 4, pp. 265-272, Jul. 1971.

[3] G. A. Covic and J. T. Boys, “Inductive power transfer,” *Proceedings of the IEEE*, vol. 101, no.6, pp. 1276-1289, Jun. 2013.

[4] S. Y. R. Hui, “Planar wireless charging technology for portable electronic products and Qi,” *Proceedings of the IEEE*, vol. 101, no.6, pp. 1290-1301, Jun. 2013.

[5] M. Treffers, “History, current status and future of the wireless power consortium and the Qi interface specification,” *IEEE Circuits & Systems Magzine*, vol. 15, no. 2, pp. 28-31, May 2015.

[6] WPC Qi: https://www.wirelesspowerconsortium.com/qi/.

[7] AirFuel Alliance: https://www.airfuel.com/.

[8] SAE TIR J2954: https://standards.sae.org/wip/j2954/.

[9] C. Jiang, K. T. Chau, C. Liu, and C. H. T. Lee, “An overview of resonant circuits for wireless power transfer,” *Energies*, vol. 10, pp. 894, Jun. 2017.

[10] W. Zhang and C. C. Mi, “Compensation topologies of high-power wireless power transfer systems,” *IEEE Trans. Veh. Electron.*, vol. 30, no. 11, pp. 6434−6445, Feb. 2015.

[11] N. Y. Kim, K. Y. Kim, J. Choi, and C. W. Kim, “Adaptive frequency with power-level tracking system for efficient magnetic resonance wireless,” *Electron. Lett.*, vol. 48, no. 8, pp. 452-454, Apr. 2012

[12] O. C. Onar, J. M. Miller, S. L. Campbell, C. Coomer, C. P. White, and L. E. Seiber, “Oak ridge national laboratory wireless power transfer development for sustainable campus initiative,” in *Proc. IEEE Transp. Electrification Conf. Expo.*, Jun. 2013, pp.1-8.

[13] Y. Yang, S. C. Tan, and S. Y. R. Hui, “Communication-free control scheme for Qi-compliant wireless power transfer system,” in *Energy Conversion Congress and Exposition (ECCE)*, Sept. 2019, pp. 4955-4960.

[14] A. Namadmalan, “Self-oscillating tuning loops for series resonant inductive power transfer systems,” *IEEE Tran. Power Electron.*, vol. 31, no. 10, pp. 7320−7327, Oct. 2016.

[15] Z. Wang, Y. Li, Y. Sun, C. Tang, and X. Lv, “Load detection model of voltage-fed inductive power transfer system,” *IEEE Tran. Power Electron.*, vol. 28, no. 11, pp. 5233−5243, Nov. 2013.

[16] Y. G. Su, H. Y. Zhang, Z. H. Wang, et. al., “Steady-state load identification method of inductive power transfer system based on switching capacitors,” *IEEE Trans. Power Electron.*, vol. 30, no. 11, pp. 6349–6355, Nov. 2015.

[17] P. Zheng, W. Lei, F. Liu, et. al., “Primary control strategy of magnetic resonant wireless power transfer based on steady-state load identification method,” in *IEEE Int. Power Electron. Appl. Conf. Expo.*, Shenzhen, China, Nov. 2018, pp. 1-5.

[18] J. Yin, D. Lin, C. K. Lee, and S. Y. R. Hui, “A systematic approach for load monitoring and power control in wireless power transfer systems without any direct output measurement,” *IEEE Tran. Power Electron.*, vol. 30, no. 3, pp. 1657−1667, Mar. 2015.

[19] J. Yin, D. Lin, C. K. Lee, T. Parisini, and S. Y. R. Hui, “Front-end monitoring of multiple loads in wireless power transfer systems without wireless communication systems,” *IEEE Tran. Power Electron.*, vol. 31, no. 3, pp. 2510−2517, Mar. 2016.

[20] J. Yin, D. Lin, T. Parisini, and S. Y. R. Hui, “Front-end monitoring of the mutual inductance and load resistance in a series-series compensated wireless power transfer system,” *IEEE Trans. Power Electron.*, vol. 31, no. 10, pp. 7339–7352, Oct. 2016.

[21] Y. Yang, Y. Jiang, S. C. Tan, and S. Y. R. Hui, “A frequency-sweep based load monitoring method for weakly-coupled series-series compensated wireless power transfer systems,” in *PELS Workshop on Emerging Technologies: Wireless Power Transfer (WoW)*, Montréal, QC, Canada, Jun. 2018, pp. 1-5.

[22] Y. Yang, S. C. Tan, and S. Y. R. Hui, “Front-end parameter monitoring method based on two-layer adaptive differential evolution for SS-compensated wireless power transfer systems,” *IEEE Trans. Ind. Informat.*, vol. 15, no. 11, pp. 6101–6113, Nov. 2019.

[23] Y. Yang, S. C. Tan, and S. Y. R. Hui, “Fast hardware approach to determining mutual coupling of series-series-compensated wireless power transfer systems with active rectifiers,” *IEEE Trans. Power Electron.*, vol. 35, no. 10, pp. 11026-11038, Oct. 2020.

[24] Y. Yang, W. Zhong, S. Kiratipongvoot, S. C. Tan, and S. Y. R. Hui, “Dynamic improvement of series-series compensated wireless power transfer systems using discrete sliding mode control,” *IEEE Tran. on Power Electron*., vol. 33, no. 7, pp. 6351-6360, Jul. 2018.

[25] H. L. Li, A. P. Hu, G. A. Covic, and C. Tang, “A new primary power regulation method for contactless power transfer,” in *Proc. IEEE Int. Conf. Ind. Technol.*, Feb. 2009, pp. 1–5.

Author Index

Submission Details

Only online submission will be accepted. Please first register and submit online. The paper is in double-column and is similar to most IET or IEEE journal formats. There is no page limit. Any number of pages of more than 6 will be subjected to an additional charge.

The paper guidelines can be downloaded using the link: http://perc.polyu.edu.hk/apejournal/

Any queries, please contact Prof. Eric Cheng, Publishing Director of APEJ, Dept. of Electrical Engineering, The Hong Kong Polytechnic University, Hung Hom, Hong Kong. Email: eeecheng@polyu.edu.hk Fax: +852-2330 1544

Any secretarial support and production related matters, please contact Dr. James Ho, Power Electronics Research Centre, The Hong Kong Polytechnic University, Hung Hom, Hong Kong. Email: eeapej@polyu.edu.hk Tel: +825-3400 3348 Fax: +852-3400 3343

Publication Details

The journal will be published 2-3 times a year. The first issue was published in 2007. Response time for paper acceptance is within 3 months.

Financial Charge

All the accepted papers will be printed without charge for 6 or less pages. An additional page charge is HK$100 per page. A hardcopy of the journal will be posted to the corresponding author free of charge. Additional copies of the journal can be purchased at HK$200 each. The charge includes postage and packing.

All Chinese Papers will be subjected to a translational fee of HK$350 per page. It will be charged when the paper is accepted for publication.

Advertising

Advertisement is welcome. Full page advertisement is HK$1000. For colour advertisements, the amount is doubled. All the advertisements will be both posted online in the journal website and hardcopy of the journal.

For advertising enquires and details, please contact Ms. Anna Chang, eeapej@polyu.edu.hk.

Tel: +852-3400 3348, Fax: +852-3400 3343

For payment, please send your cheque, payable to ‘The Hong Kong Polytechnic University, address to Ms. Kit Chan, Secretary of APEJ, Dept. of Electrical Engineering, The Hong Kong Polytechnic University, Hung Hom, Hong Kong.’